Spring 2009

Self similar flows in finite or infinite two dimensional geometries

Leonardo Xavier Espin Estevez
New Jersey Institute of Technology

ABSTRACT

SELF SIMILAR FLOWS IN FINITE OR INFINITE TWO DIMENSIONAL GEOMETRIES

by
Leonardo Xavier Espín Estevez

This study is concerned with several problems related to self-similar flows in pulsating channels. Exact or similarity solutions of the Navier-Stokes equations are of practical and theoretical importance in fluid mechanics. The assumption of self-similarity of the solutions is a very attractive one from both a theoretical and a practical point of view. It allows us to greatly simplify the Navier-Stokes equations into a single nonlinear one-dimensional partial differential equation (or ordinary differential equation in the case of steady flow) whose solutions are also exact solutions of the Navier-Stokes equations in the sense that no approximations are required in order to calculate them. One common characteristic to all applications of self-similar flows in real problems is that they involve fluid domains with large aspect ratios. Self-similar flows are admissible solutions of the Navier-Stokes equations in unbounded domains, and in applications it is assumed that the effects of the boundary conditions at the edge of the domain will have only a local effect and that a self-similar solution will be valid in most of the fluid domain. However, it has been shown that some similarity flows exist only under a very restricted set of conditions which need to be inferred from numerical simulations. Our main interest is to study several self-similar solutions related to flows in oscillating channels and to investigate the hypothesis that these solutions are reasonable approximations to Navier-Stokes flows in long, slender but finite domains.

SELF SIMILAR FLOWS IN FINITE OR INFINITE TWO DIMENSIONAL GEOMETRIES

by
Leonardo Xavier Espín Estevez

A Dissertation
Submitted to the Faculty of
New Jersey Institute of Technology and
Rutgers, The State University of New Jersey - Newark
in Partial Fulfillment of the Requirements for the Degree of
Doctor of Philosophy in Mathematical Sciences

Department of Mathematical Sciences, NJIT
Department of Mathematics and Computer Science, Rutgers-Newark

May 2009

APPROVAL PAGE

SELF SIMILAR FLOWS IN FINITE OR INFINITE TWO DIMENSIONAL GEOMETRIES

Leonardo Xavier Espín Estevez

4/29/2009

Dr. Demetrios Papageorgiou, Dissertation Advisor — Date
Professor of Mathematics, NJIT

4/29/09

Dr. Linda J. Cummings, Committee Member — Date
Associate Professor of Mathematics, NJIT

4/29/2009

Dr. Peter G. Petropoulos, Committee Member — Date
Associate Professor of Mathematics, NJIT

4/29/09

Dr. David Rumschitzki, Committee Member — Date
Professor of Chemical Engineering, City College of New York

4/29/09

Dr. Michael Siegel, Committee Member — Date
Professor of Mathematics, NJIT

BIOGRAPHICAL SKETCH

Author: Leonardo Xavier Espín Estevez

Degree: Doctor of Philosophy

Date: May 2009

Undergraduate and Graduate Education:

- Doctor of Philosophy in Mathematical Sciences,
  New Jersey Institute of Technology, Newark, New Jersey, 2009
- Master of Science in Applied Mathematics,
  New Jersey Institute of Technology, Newark, New Jersey, 2008
- Master of Science in Applied Mathematics,
  National Institute of Pure and Applied Mathematics, Rio de Janeiro, Brazil, 2003
- Bachelor of Science in Mathematics,
  Escuela Politécnica Nacional, Ecuador, 2001

Major: Mathematical Sciences

Dedicado a Gabriela y a mis padres Xavier y Ximena. Es gracias a ustedes que he podido llegar hasta aquí.

Dedicated to Gabriela and my parents Xavier and Ximena. It is because of you that I have been able to reach this point.

ACKNOWLEDGMENT

I want to thank professor Demetrios Papagergiou for his invaluable advice, his patience and for his sincere interest in me and my development as a scientist. I have learned from him that part of being a good scientist is also being a good communicator, and I have to say that it is very difficult to become one. I want to thank professors Michel Siegel, Linda Cummings, Peter Petropoulos and David Rumschitzki for being my thesis committee members and also for their patience, particularly those who read the first draft of this document two years ago. I want to thank the entire department of mathematical sciences and specially professors Gregory Kriegsmann, Louis Tao, Robert Miura, Wooyoung Choi and Sheldon Wang for their help during my time at the department. I would also like to thank Professor Andre Nachbin from IMPA, who gave me the idea of coming to NJIT. Finally I want to thank Jeff Grundy and the excellent department of International Students of NJIT which is, precisely, one of the good things about being an international student here at NJIT.

TABLE OF CONTENTS

TABLE OF CONTENTS

(Continued)

Chapter **Page**

LIST OF TABLES

Table **Page**

LIST OF FIGURES

Figure **Page**

LIST OF FIGURES
(Continued)

Figure **Page**

LIST OF FIGURES
(Continued)

Figure **Page**

CHAPTER 1

INTRODUCTION

The incompressible Navier-Stokes equations govern the motion of viscous fluids and in a two dimensional Cartesian coordinate system take the following form:

$$\rho(u_t + uu_x + vu_y) = -p_x + \mu(u_{xx} + u_{yy}), \tag{1.1}$$

$$\rho(v_t + uv_x + vv_y) = -p_y + \mu(v_{xx} + v_{yy}), \tag{1.2}$$

$$u_x + v_y = 0, \tag{1.3}$$

where u and v denote the horizontal and vertical components of the velocity field of the fluid and p is the pressure. These three unknowns depend on the spatial variables x, y and time t. The parameters ρ and μ represent the density and the viscosity of the fluid respectively. The Navier-Stokes equations result from applying the *Transport Theorem* to the integral form of the equations of balance of momentum and incompressibility of the fluid (see Chorin and Marsden (1992)). This study is concerned with several problems related to self-similar flows in pulsating channels, that is we are interested in a particular class of solutions of equations (1.1)-(1.3) for channel geometries.

Exact or similarity solutions of the Navier-Stokes equations are of practical and theoretical importance in fluid mechanics. In addition to direct physical applications, they serve as benchmarks for the validity of complex numerical codes. Many basic flows studied in the field of fluid dynamics are of exact or similarity form: Poiseuille flow in a pipe, stagnation-point flows, rotating-disk flows are some examples (for a recent and extensive review of exact solutions of the Navier-Stokes equations the reader is referred to the monograph by Drazin and Riley (2006)). The assumption of self-similarity of the solutions is a very attractive one from both a theoretical and a practical point of view. It allows us to greatly simplify the equations of motion (1.1)-(1.3) into a single nonlinear one-dimensional

partial differential equation (or ordinary differential equation in the case of steady flow) whose solutions are also exact solutions of the Navier-Stokes equations in the sense that no approximations are required in order to calculate them.

Self-similar flows have been widely used in applications. A few of them, which are related to this study are: a model of gas transport in the airways of the lung (Hydon and Pedley 1993), a model for oxygen transport in transmyocardial revascularization channels or tubes (Waters 2001), (Waters 2003), a model of blood flow in coronary arteries (Secomb 1978) and flows in porous channels or tubes (Brady 1984). One common characteristic to all applications of self-similar flows in real problems is that they involve fluid domains with large aspect ratios. Self-similar flows are admissible solutions of the Navier-Stokes equations in unbounded domains, and in all the applications mentioned it is typically assumed that the effects of the boundary conditions at the edge of the domain will have only a local effect and that a self-similar solution will be valid in most of the fluid domain. However, it has been shown that some similarity flows exist only under a very restricted set of conditions which need to be inferred from numerical simulations (see for example Brady and Acrivos (1982*a*), Brady (1984), Hewitt and Hazel (2007)). Our main interest is to study several self-similar solutions related to flows in oscillating channels and to investigate the hypothesis that these solutions are reasonable approximations to Navier-Stokes flows in long, slender but finite domains.

In Chapter 2, we compare channel flows driven by accelerating (and decelerating) surface velocity in finite, slender channels with the self-similar solution which exist in infinite channels. There is a direct connection between channel flows driven by decelerating surface velocity and channel flows driven by vertically oscillating walls since the former arises from the latter in a distinct high-frequency small amplitude limit identified and analyzed by Hall and Papageorgiou (1999).

Chapter 3 is concerned with flows driven by pulsating channels. Secomb (1978), studied the flow driven by a two-dimensional infinite channel whose parallel walls oscillate

vertically in a prescribed way. He considered the limiting cases of low and high-frequency wall oscillations, and also the case of small amplitude wall oscillations for arbitrary frequency. Hall and Papageorgiou (1999) studied a closely related problem and presented results for arbitrary oscillation frequencies and amplitudes. They found that the dynamics of the flow depend on two non-dimensional parameters: the dimensionless amplitude of the wall oscillation, Δ, and the Reynolds number of the flow, R (see Section 3.2.1 for a summary of the main results concerning this flow). In Section 3.2, we study a secondary flow which results by superimposing a pressure gradient to the flow driven by vertically oscillating walls described in Section 3.2.1. We find that the dynamics of the secondary flow are very different from that of the pulsating flow. In particular, we find that for any value of the oscillation amplitude a bifurcation occurs at a critical Reynolds number above which the flow transitions from a time-periodic state to solutions that grow exponentially in time. In contrast with the pulsating flow, a symmetry breaking bifurcation may or may not occur, depending on the value of the oscillation amplitude. In Section 3.4 we generalize the similarity flow driven by vertically oscillating walls by allowing the channel walls to move laterally as well. This flow is related to an application in passive solute transport and diffusion in an oscillating channel which is studied in Chapter 4. In Section 3.6 we compare the similarity flow of Section 3.4 with flows admitted in finite, truncated domains computed by solving the Navier-Stokes equations numerically.

In Chapter 4 we study a model for oxygen transport in revascularization channels which utilizes a self-similar solution as a model flow for the fluid inside the channel. The transmyocardial laser revascularisation procedure is a surgical technique consisting of drilling long narrow tunnels in certain parts of the heart with the purpose of bringing oxygenated blood to the heart muscle. Waters (2001) used asymptotic techniques to determine the effects of the fluid flow on the delivery of solute to the walls of a two dimensional pulsating channel by deriving an asymptotic solution in the double limit of small amplitude oscillations and large Péclet number. We perform a numerical study of the model proposed

by Waters (2001) for a broader range of the non-dimensional parameters. Specifically, we study how the approximation is affected when the amplitude of the wall oscillation increases and we find an approximate range for which the asymptotic approximation and the numerical approximation give comparable results. We conclude by outlining possible extensions of this study and describe future research directions.

CHAPTER 2

CHANNEL FLOWS DRIVEN BY ACCELERATING SURFACE VELOCITY

2.1 Introduction

In this Chapter we compare the numerically computed solutions of Navier-Stokes flow in a channel of finite length, driven by the accelerating surface velocity of the channel walls (which we call 'accelerating wall' driven flow), with the self-similar solution admitted by the respective problem in an infinitely long channel. We are interested in studying how the similarity solution is captured as a Navier-Stokes flow in a truncated domain, and how the rich bifurcation structure of this class of self-similar solutions is affected by a truncated domain (for example it has been shown that these similarity flows can produce complex dynamics including chaotic behavior that follows a Feigenbaum period-doubling scenario at order one values of the driving parameters, see Hall and Papageorgiou (1999), Feigenbaum (1981)). In addition we formulate and solve linear stability problems of the self-similar solutions to general perturbations in order to explain any discrepancies between computed and self-similar solutions. Previous work (e.g. Brady (1984), Brady and Acrivos (1981), Brady and Acrivos (1982*a*)) has shown that similarity flows may not describe a realizable flow accurately, even if only localized regions of the domain of the problem are considered. Also, the recent work by Hewitt and Hazel (2007) has shown that non-linear perturbations at the edge of the finite domain can significantly alter the bifurcation structure of a similarity flow, as well as the bifurcated solutions. As we will show, similarity flows could become linearly unstable, rendering the self-similar solution irrelevant in finite channels after a critical value of the Reynolds number is crossed.

In Section 2.2 we introduce the equations of the problem, the scalings and conventions we utilize through this Chapter. In Section 2.3 we give a brief description of the code we use to compute our numerical solutions and in Section 2.4 we present our results.

Section 2.5 is left for a discussion and conclusions.

2.2 Mathematical Formulation

Consider a rectangular channel of semi-width a and length $2L$ filled with a viscous incompressible fluid of density ρ and viscosity μ. The top and bottom walls move with the following velocity parallel to the x-axis

$$u(x,\pm a) = Ex, \quad v(x,\pm a) = 0, \tag{2.1}$$

where E is a constant with units of inverse time. In equation (2.1) and in the rest of this Chapter, we use a Cartesian coordinate system (x,y) with the origin placed at the center of the channel so that the walls are given by $y = \pm a$, and the channel ends are at $x = \pm L$. The corresponding velocity field is denoted by $\mathbf{u} = (u,v)$. Since the velocity due to the accelerating wall is symmetric about the plane $x = 0$, it is sufficient to solve in the region $x > 0$ with symmetric boundary conditions imposed at $x = 0$. At the edge $x = L$ the fluid is allowed to enter and leave the channel and the boundary conditions to be imposed there are discussed in detail later. We emphasize that the edge boundary conditions are central to our study since they affect the flow in the whole domain and in particular dictate whether a similarity solution emerges or not - see later. A schematic of the flow geometry is provided in figure 2.1.

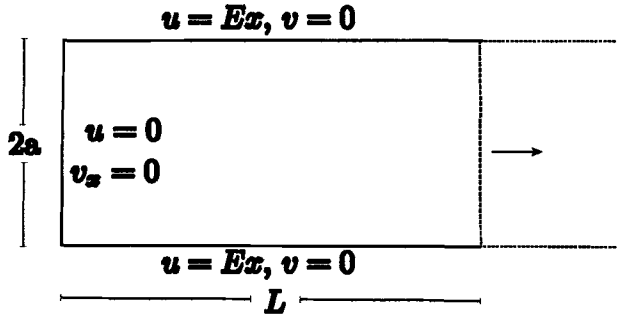

Figure 2.1 Schematic diagram for the flow in a long, slender channel with accelerating walls.

The length of the channel, L, and its semi-width a provide a natural way for defining dimensionless variables for this problem. Accordingly we set

$$x' = \frac{x}{L}, \quad y' = \frac{y}{a}, \quad t' = Et, \quad u' = \frac{u}{EL}, \quad v' = \frac{v}{Ea}, \quad p' = \frac{a^2 p}{L^2 \mu E},$$

which leads to the nondimensional Navier-Stokes equations (after dropping the primes)

$$u_t + uu_x + vu_y = -\frac{1}{R}p_x + \frac{1}{R}(\varepsilon^2 u_{xx} + u_{yy}), \tag{2.2}$$

$$v_t + uv_x + vv_y = -\frac{1}{\varepsilon^2 R}p_y + \frac{1}{R}(\varepsilon^2 v_{xx} + v_{yy}), \tag{2.3}$$

$$u_x + v_y = 0, \tag{2.4}$$

where $R = \rho E a^2/\mu$ is the Reynolds number for the flow, and the reciprocal of the aspect ratio of the channel is $\varepsilon = a/L$. The boundary conditions (2.1) at the symmetry plane $x = 0$ and at the walls $y = \pm 1$ become

$$\begin{aligned} u(0,y) &= 0, \qquad v_x(0,y) = 0 \\ u(x,\pm 1) &= x, \qquad v(x,\pm 1) = 0. \end{aligned} \tag{2.5}$$

The boundary conditions at the scaled channel end $x = 1$ are left unspecified until Section 2.3 where they are required for the calculation of numerical solutions. In the case of negative acceleration, the only change is in the boundary conditions $u(x,1) = u(x,-1) = -x$. By simplicity and for historical reasons (see Watson et al. (1990), Brady and Acrivos (1981)), we will refer to this case as negative Reynolds number flow.

The problem (2.2)-(2.4) is exact and is solved numerically later. In the limiting case when $\varepsilon \to 0$ (or equivalently when $L \to +\infty$, i.e. the geometry becomes infinite), the equations admit a similarity solution of the form

$$u = x f_y(y,t), \qquad v = -f(y,t), \qquad p = \frac{\beta}{2}x^2 + p_0(y), \tag{2.6}$$

that arises from the stream function $\psi(x,y,t) = xf(y,t)$ for the flow. The function $f(y,t)$ satisfies the equation

$$f_{yyt} = ff_{yyy} - f_y f_{yy} + \frac{1}{R} f_{yyyy}, \tag{2.7}$$

subject to the no-slip boundary conditions at the walls

$$f_y(\pm 1,t) = 1, \qquad f(\pm 1,t) = 0. \tag{2.8}$$

The constant pressure coefficient β and the pressure $p_0(y)$ appearing in (2.6) can be calculated from the equations of motion (2.2)-(2.4) once $f(y,t)$ has been determined.

Our objective is to study the relation between the similarity solution f with the Navier-Stokes flow described by (2.2)-(2.5) in the case $\varepsilon > 0$. Even though any value of ε can be taken in a direct numerical simulation, it is appropriate to consider small values of ε corresponding to long channels. There are two reasons for this: first, we want the channel to be sufficiently long so that different conditions at $x = 1$ (recall that in unscaled terms the channel length is $1/\varepsilon$) have sufficient distance to adjust to the exact similarity solution (2.6); second, a long channel enables us to also study via our full simulation, the spatial stability of the exact solutions at different values of the flow parameters. Both of these are addressed fully in what follows. Brady and Acrivos (1982*a*) studied the related problems of a symmetric flow (about the x-axis) in a closed channel or tube, driven by the accelerating walls of an asymptotically infinite channel or tube. They found that below a critical value of the Reynolds number, small perturbations to the similarity velocity profiles at the channel edge will decay to zero and consequently the similarity solution would be a good approximation to the flow in a range $0 \leq x \leq x_0 < 1$ which depends on R. Above this critical value, the perturbations at the edge propagate to the interior of the channel and affect the solution in the whole domain, fundamentally altering its nature. In our case, the channel is of finite extent and we do not impose symmetry along the channel center-line ($y = 0$) since, as seen by Watson et al. (1990), the asymmetric branch of the similarity

solution f presents a richer bifurcation structure than the symmetric branch at moderately large values of the Reynolds number, and is also more strongly attracting since it is stable at the higher Reynolds numbers.

2.3 Numerical Methods

In order to compare the exact solution described by (2.7)-(2.8) with the flow in a long, finite channel with aspect ratio $0 < \varepsilon \ll 1$, we set $\varepsilon = 1/100$ (corresponding to a channel 100 times longer than wide) and solve equations (2.2)-(2.4) subject to boundary conditions (2.5) plus conditions at the channel edge at $x = 1$. We consider two different cases: outflow conditions

$$u_x(1,y,t) = v_x(1,y,t) = 0, \tag{I}$$

and inflow conditions which consist of prescribing the exact self-similar solution at the edge

$$u(1,y,t) = f_y(y,t), \qquad v(1,y,t) = -f(y,t). \tag{II}$$

Conditions of type (I) are non-linear perturbations of the self-similar flow which allow us to compare the behavior of this flow with the findings reported by Hewitt and Hazel (2007) in a different problem of the flow between two counter rotating disks. As in the present case, that flow admits self-similar solutions of stagnation point type when the disks are of infinite radius.

Type (I) conditions require that the total velocity does not change in the direction normal to the end of the channel. Conservation of mass is automatically satisfied for type (II) conditions, and for type (I) conditions it implies that $v(x = 1,y,t) = 0$, which is imposed accordingly. We solve equations (2.2)-(2.5) numerically with a finite differences scheme based on the projection method of Chorin that is described in the book by Griebel et al.

(1998). We describe our numerical method in detail in Appendix A. Unless stated otherwise, the initial condition for the Navier-Stokes computations is taken to be a quiescent state throughout the channel and marching is used to reach the most attracting states of the initial-boundary value problem. Such initializations are appropriate when making comparisons between the steady branches of the similarity equations and their Navier-Stokes analogues. For our computations involving unsteady time-periodic branches, we integrate the self-similar system (2.7)-(2.8) to large enough times so that transients die away (in many cases this requires integrations larger than 1000 time units), and the self-similar solutions obtained supply the initial conditions in the whole channel, for the Navier-Stokes computation. Beyond this initialization, the two systems (self-similar and Navier-Stokes) are solved in conjunction because they couple through the end conditions at $x = 1$.

We use two different methods to solve the similarity equations (2.7)-(2.8). The first one consists of solving the steady version of equation (2.7) in order to obtain solution branches that may not be stable. This nonlinear boundary value problem was solved with MATLAB's *bvp4c* solver. For values of R larger than approximately 355, where the exact solution f becomes time dependent due to a Hopf-bifurcation, we use a time-dependent, finite differences code based on the algorithm described by Hall and Papageorgiou (1999) (as pointed out in the introduction, the problem studied in (Hall and Papageorgiou 1999) and the one described by equations (2.7)-(2.8) are closely related and the numerical method utilized in that paper can be easily modified to solve (2.7)-(2.8)). The unsteady code is capable of calculating the most attracting stable solution since it is based on the solution of an initial value problem. Solutions which are symmetric or non-symmetric about the x-axis are computed throughout in order to make full comparisons with the Navier-Stokes solutions.

2.4 Results

When conditions of type (I) are used, our computations indicate that the solution always reaches a steady state after a sufficiently large integration time. This integration time increases with increasing Reynolds number - for example, the integration times required to attain a steady state for the results in Figure 2.2 at Reynolds numbers 0, 100, 300 and 500 are about 10, 40, 340, and 670, respectively.

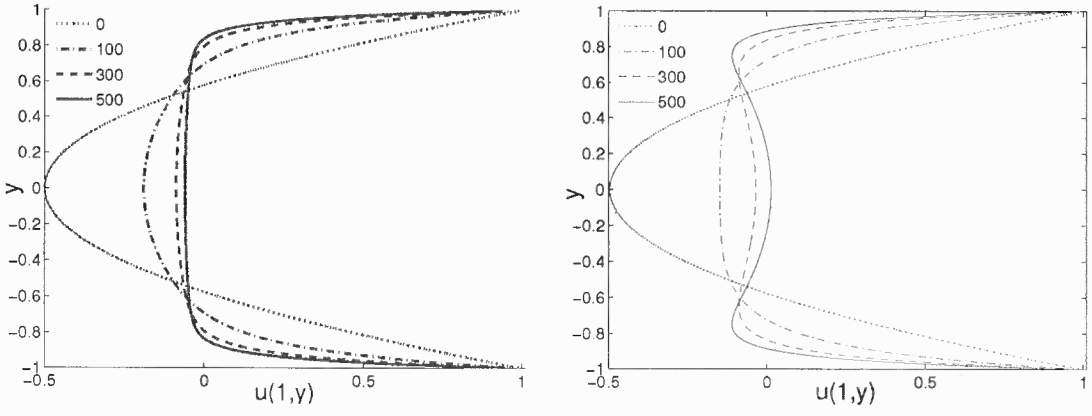

Figure 2.2 (a) Velocity profiles obtained from the symmetric branch of the exact solution f and (b) type (I) velocity profiles at the channel edge $x = 1$ for several values of the Reynolds number. The aspect ratio of the channel is $\varepsilon = 0.01$.

When R is small, type (I) numerical solutions agree with the exact solution in the entire domain (i.e. for all $0 \leq x < 1$) but the range where agreement is obtained decreases with increasing R. This can be observed by comparing the velocity profiles at the channel edge shown in Figure 2.2(b) with the corresponding profiles obtained from the steady exact solution $f(y)$ shown in Figure 2.2(a). A comparison of the exact and computed pressure gradient over the whole extent of the channel provides a global measure of the differences between the simulations and exact Navier-Stokes solutions. Figure 2.3 depicts the pressure gradient $\partial p/\partial x(x, y = 0)$ computed from the numerical solution and a straight dash-dot line $dp/dx = x\beta(R)$ obtained from the exact solution (2.6), both calculated when $R = 100$. Results obtained with boundary conditions of type (I) and (II) are shown by the labeled curves (a) and (b), respectively. At this value of the Reynolds number type (I) conditions

support a region near $x = 0$ where the Navier-Stokes flow coincides with the exact solution, while for type (II) conditions the region of almost perfect agreement is over 70% of the channel length. To emphasize this agreement we use the velocity profiles computed from the Navier-Stokes code at different values of $x = x_i$, say, and construct the exact solution analogues using the self-similar forms (2.6). More precisely we construct the velocity profiles $v(x_i, y)$ and $u(x_i, y)/x_i$ for several values of x_i in the range of agreement, $0 < x \leq 0.19141$ for type (I) conditions and $0 < x \leq 0.91797$ for type (II) conditions as indicated by the results of Figure 2.3. The results are shown collectively in Figure 2.4 with the top panels corresponding to type (II) conditions and the bottom ones to type (I) conditions. As shown, both computed solutions are self-similar and identical in the regions described in the Figure. We note that there are approximately 250 profiles superimposed in the type (II) top panels, and about 50 profiles in the lower type (I) panels. For completeness we also superimpose the exact solutions given by (2.6) at $R = 100$ indicating that the Navier-Stokes equations in a finite domain produce this exact solution.

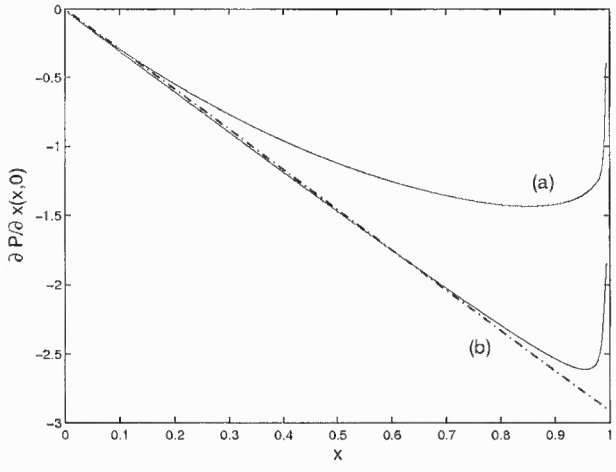

Figure 2.3 Pressure gradients $\partial P/\partial x(x, 0)$ for (a) type (I) numerical solution and (b) type (II) solution, computed when $R = 100$. The dashed straight line was computed from the similarity solution (2.6). The aspect ratio of the channel is $\varepsilon = 0.01$.

The remaining fraction of the domain where the flow adapts to the self-similar profile can be significantly reduced in the case of type (II) solutions, by increasing the number of discretization points. Considering the corresponding increase in computation time we

only use the resolution necessary to correctly resolve each case presented in time and space. As reported by Hewitt and Hazel (2007) and also by Brady and Acrivos (1982*a*), in cases of self-similar flows in finite domains where type (II) conditions were subject to non-linear perturbations, the length of this 'adaptation region' has been seen to be independent of the type of perturbation used and also independent of the aspect ratio in terms of the scaled variables. We refer the reader to their papers for details about their results.

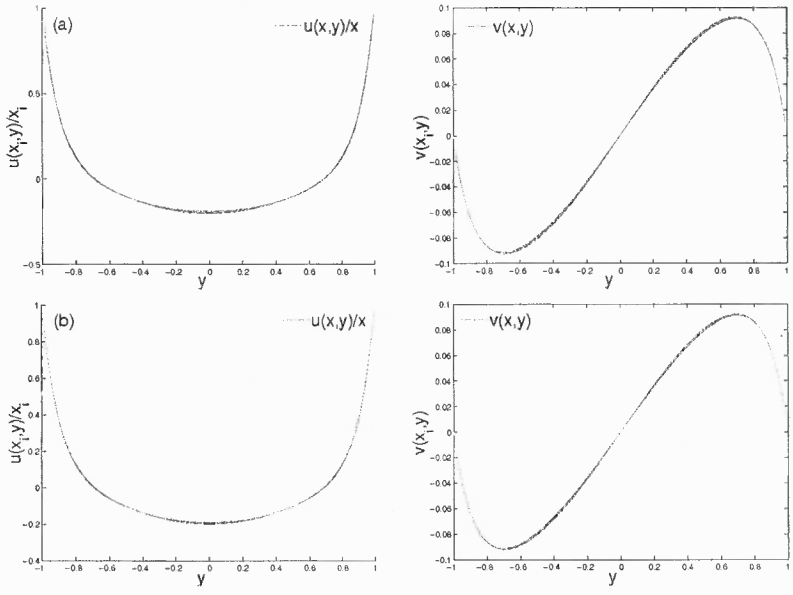

Figure 2.4 Velocity profiles corresponding to (a) type (II) edge conditions in the range $0.035156 \leq x \leq 0.91797$, (b) type (I) conditions in the range $0.035156 \leq x \leq 0.19141$ computed when $R = 100$. The aspect ratio of the channel is $\varepsilon = 0.01$.

An important difference between the flow driven by accelerating walls and the flow driven by counter rotating disks studied by Hewitt and Hazel (2007) is that for moderately large values of the Reynolds number, although symmetry is not imposed, type (I) flows remain symmetric and are significantly different from the corresponding similarity flows. This can be seen in in Figure 2.2 where reversed flow at the center-line $y = 0$ appears when $R = 300$ and 500. In the latter case the reversed flow is present in the whole channel, and the velocity profiles are similar to the one shown in the Figure, all the way down to $x = 0$. Consequently, at these values of the Reynolds number the symmetric similarity solution does not constitute a good qualitative predictor of the flow. In the case of counter

rotating disks it was reported by Hewitt and Hazel (2007) that different edge conditions could significantly alter the location of the mid-plane symmetry-breaking bifurcation, but such bifurcation was always present. Nevertheless, our results for type (I) conditions appear to confirm the conclusion presented by Hewitt and Hazel (2007) that the symmetric branch of the similarity solution is a good predictor of the flow in a vicinity of $x = 0$ for moderate values of the Reynolds number (meaning in the present context $R \lesssim 200$), independently of the boundary conditions used at the edge of the domain.

We now turn our attention to type (II) flows and their bifurcations. As found by Watson et al. (1990), when symmetry is not enforced at the channel center-line, the similarity solution has a symmetry breaking bifurcation at the critical value $R = 132.75849$ where two stable asymmetric solutions appear (each of them can be obtained by reflection about $y = 0$ from the other). Then, at the value $R = 355.5738$ the flow Hopf bifurcates and a stable, unsteady and time-periodic solution appears. The period of the unsteady solution increases with R, and it nearly doubles when $R = 400$. Eventually, when $R = 1200$ there is evidence of chaotic behavior; see (Watson et al. 1990).

In order to investigate how these features of the exact solution are replicated by our numerical solution, we performed computations with type (II) boundary conditions at the channel edge. The profiles required for imposing type (II) conditions were computed in two ways: a stable asymmetric branch of the exact solution is found by time-marching the unsteady code described in Section 2.3. Other steady solution branches are efficiently calculated with MATLAB's *bvp4c* solver for boundary value problems as mentioned earlier by using continuation methods in the Reynolds number R.

Both branches of the similarity solution, symmetric and asymmetric, are recovered by our Navier-Stokes code. In Figure 2.5 we show the pressure gradient $\partial p/\partial x(x, y = 0)$ computed from the numerical solution for type (I) and type (II) edge conditions, for the symmetric and asymmetric branches. As pointed out previously, the deviation from the line βx at the edge decreases when more discretization points are used. Further inside the

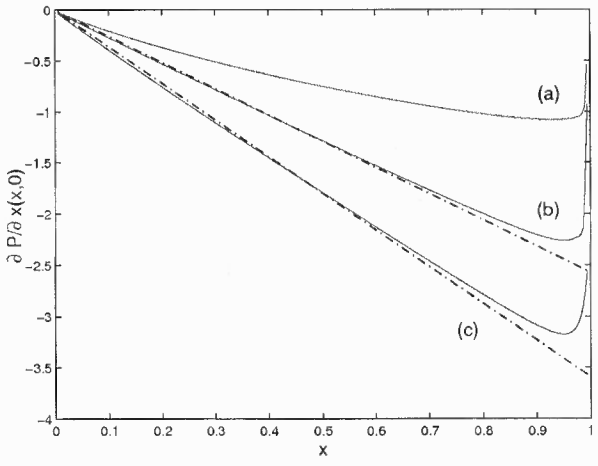

Figure 2.5 Pressure gradients $\partial P/\partial x(x,0)$ for (a) type (I) solution and (b)-(c) type (II) solutions in the case $R = 200$. The type (II) edge condition for (b) came from the symmetric branch of the similarity solution and the edge condition for (c) came from an asymmetric branch. Dash-dot lines were obtained from the similarity solution f in the respective cases. The aspect ratio of the channel is $\varepsilon = 0.01$.

channel, as the fluid moves away from the edge the solution decays to the similarity solution as evidenced by the results of Figure 2.6 where profiles $v(x_i, y)$ and $u(x_i, y)/x_i$ for values of x_i between 0 and $x = 0.9179$ are superimposed with the exact solution velocity profiles. Similar results are obtained for larger values of R. As an example, in Figure 2.7 we show pressure gradients corresponding to the asymmetric branch of f, for several values of the Reynolds number in the regime $R \geq 345$.

2.4.1 Unsteady Solutions

When $R = 355.5738$ the asymmetric steady branch of (2.7) Hopf bifurcates and a time periodic solution arises. We can impose time dependent type (II) conditions by solving (2.7) numerically as explained in Section 2.3 and then coupling this solution to our Navier-Stokes solver.

When the Reynolds number is 370 the time dependent exact solution has an approximate period of 199. As can be observed in Figure 2.8 where velocity profiles near $x = 0$ and $x = 1$ are compared at two instants of time, the exact solution changes slowly over time

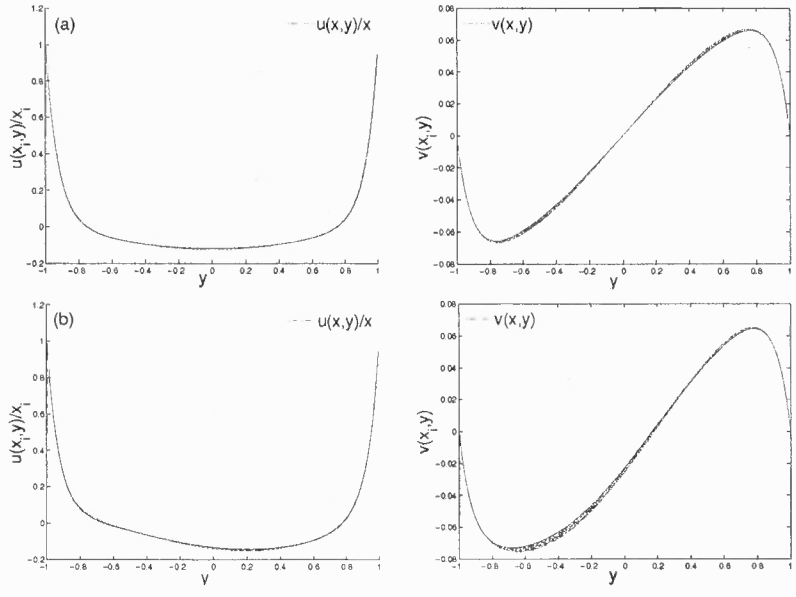

Figure 2.6 Type (II) velocity profiles corresponding to (a) symmetric branch of the exact solution, (b) asymmetric branch for $0.074219 \leq x \leq 0.91797$ in the case $R = 200$. The aspect ratio of the channel is $\varepsilon = 0.01$.

and this allows the numerical solution to adapt to the time dependent conditions at the edge. This slow time variation turns out to be fundamental for the stability of the flow as will be explained in the next paragraphs. Due to the proximity with the location of the Hopf bifurcation, the self-similar solution requires a long time to converge to a periodic state. This explains the relatively large variation between the profiles near $x = 1$ and $x = 0$ at the time $t = 1949.968$. When $R = 500$ the agreement between the Navier-Stokes solution and the self-similar solution has improved within the same range of time as can be seen in Figure 2.9. In the right panel of Figure 2.9 we show the velocity signals $u(x = 1/2, y = 0, t)$, with a solid line, and $f_y(y = 0, t)/2$ with a dash-dot line. The lag between the two curves indicates the time that it takes the information prescribed as type (II) edge condition to reach the middle of the channel.

As the Reynolds number increases, the lag that occurs between type (II) conditions and the velocities at the interior of the channel destabilizes the self-similar flow. When $u(1/2, 0, t)$ reaches a minimum, the acceleration changes sign and as seen in Figure 2.10 the change of sign for $f_{yt}(0, t)$ occurs at a later time, producing small oscillations. At the

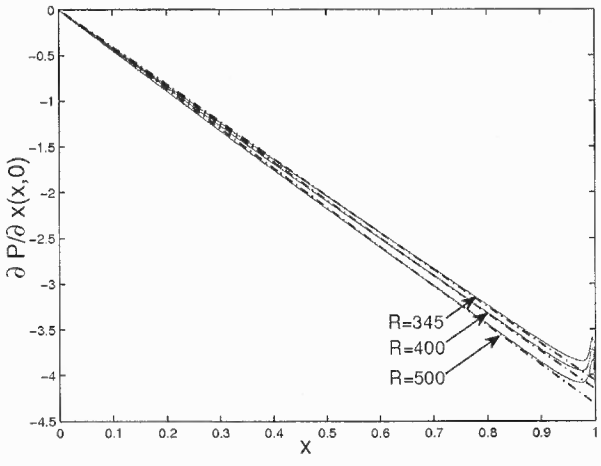

Figure 2.7 Pressure gradients at the channel center line computed from type (II) solutions at different values of the Reynolds number. The dash-dot lines were obtained from the exact solution of the asymmetric branch in the respective cases. The aspect ratio of the channel is $\varepsilon = 0.01$.

top, left panel we can see a 34% increase in the total kinetic energy of the flow, occurring after f_{yt} has changed sign. When $R = 900$, the flow is no longer periodic, although the Navier-Stokes solution coincides with the self-similar solution during periods of time when the kinetic energy of both solutions is smaller. When the kinetic energy is the smallest, the self-similar solution is symmetric or nearly symmetric. This is an attracting mode, which stabilizes the Navier-Stokes solution, in a similar way to what is shown in Figure 2.8, where profiles at time $t = 4261.556$ are nearly symmetric throughout the channel. This results in a return of the Navier-Stokes flow to a 'initial' symmetric state which is then forced by a periodic type (II) condition producing identical oscillations. This cycle is repeated resulting in a Navier-Stokes flow which is periodic but not self-similar, as in the cases $R = 600$, 700 and 800 (approximate periods are reported in Table 2.1). Increasing the Reynolds number further results in global instability of the self-similar flow, with oscillations persisting in time and propagating over the whole domain as in Figure 2.13. See the linear stability analysis of Section 2.4.3 for details about the stability of the different branches of the exact solution.

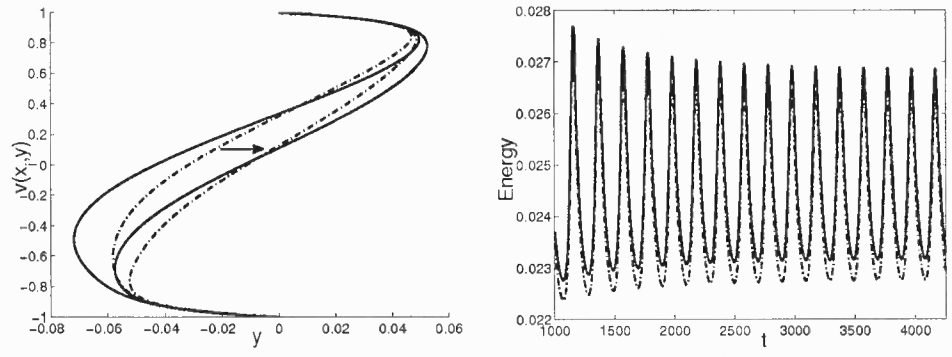

Figure 2.8 Vertical velocity profiles at $x = 0.004$ (solid line) and $x = 0.93359$ (dash-dot line) at two different times: $t = 1949.968$ and $t = 4261.556$ in the case $R = 370$. The arrow shows the direction of increasing time. The right hand plot shows the kinetic energy of the solution (solid line) as a function of time. The dash-dot line is the energy of the exact solution. The aspect ratio of the channel is $\varepsilon = 0.01$

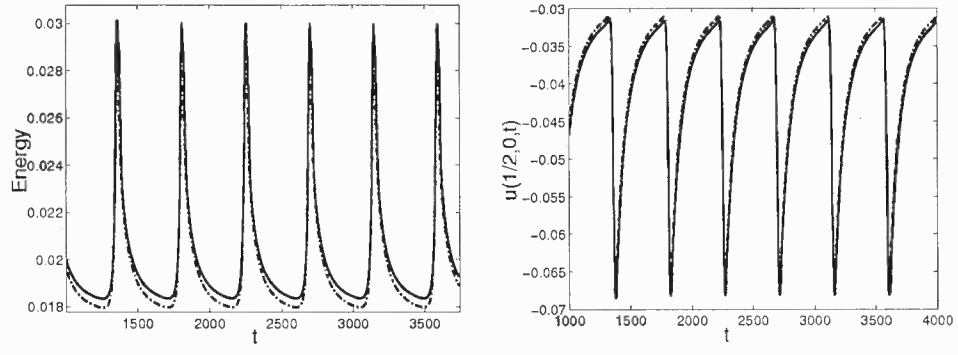

Figure 2.9 In the left panel we show a plot of the kinetic energy of the Navier-Stokes solution (solid line) as a function of time. The dash-dot line is the energy of the exact solution. At the right panel we show velocity signals $u(x = 1/2, y = 0, t)$ (solid line) and $f_y(y = 0, t)/2$ (dash-dot line). All quantities where computed in the case $R = 500$. The channel aspect ratio is $\varepsilon = 0.01$

2.4.2 Decelerating Wall Flows, $E < 0$

In the case of decelerating walls, the similarity solution f is an odd function of y for values of R less than the critical value 17.30715 where there is a symmetry breaking bifurcation. The asymmetric solutions which appear from this bifurcation are time independent until they Hopf-bifurcate at the critical value $R = 55.77$. As found by Watson et al. (1990), increasing the Reynolds number further results in a period doubling cascade with evidence of chaos at the value $R \approx 78.7$.

We proceed with our computations as we did in the case $E > 0$ by using type (II)

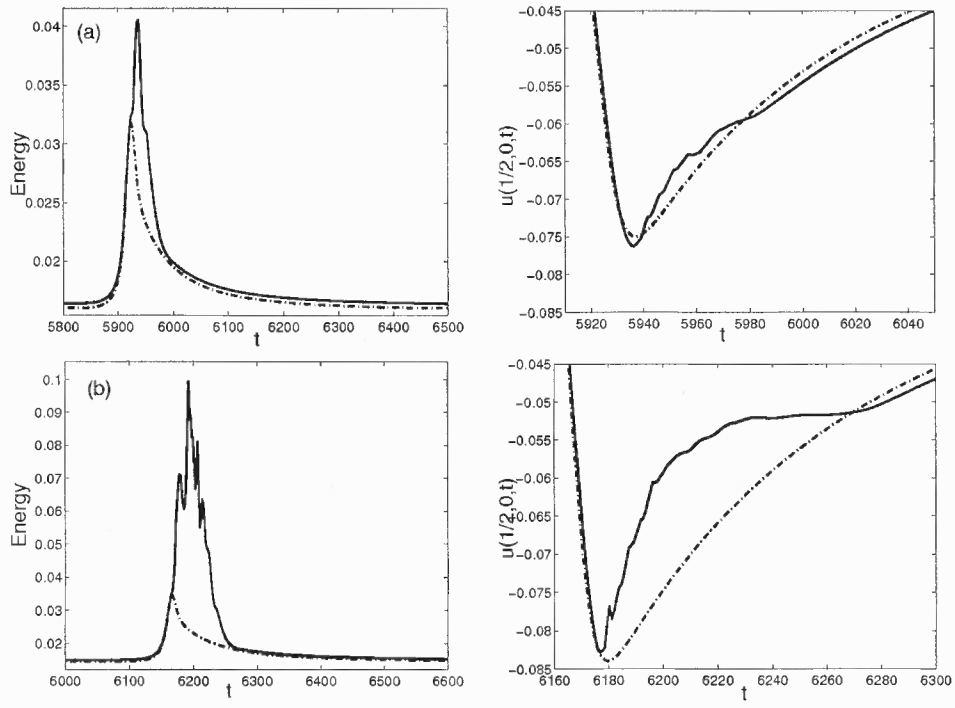

Figure 2.10 In the left panels we show plots of the kinetic energy of the Navier-Stokes solution (solid line) as function of time. The dash-dot lines are the energy of the exact solution. At the right panels we show velocity signals $u(x = 1/2, y = 0, t)$ (solid line) and $f_y(y = 0, t)/2$ (dash-dot line) computed when (a) $R = 600$ and (b) $R = 700$. The channel aspect ratio is $\varepsilon = 0.01$

conditions which were obtained from the steady asymmetric branch of f. In Figure 2.11 we show pressure gradients $\partial p/\partial x(x, y = 0)$ computed when $R = 15$, 45 and 57. The similarity solution is recovered in the whole channel in the case $R = 15$, but only away from the channel ends for the other two cases, since a collision region forms near $x = 0$. In this region of the channel the flow is not of similarity form as can be seen in Figures 2.11 and 2.12.

Further investigation of the formation of these collision regions have led us to conclude that both steady branches of the exact solution f, symmetric and asymmetric, are unstable to spatial perturbations in the negative Reynolds number case, when R is larger than a critical number $R_0 \approx 33$. Below this value, perturbations to type II conditions will grow as the fluid travels down the channel resulting in the collision regions observed around $x = 0$. When the Reynolds number is large a sufficient amount of fast moving fluid enter-

Table 2.1: Approximate period of time dependent type (II) solutions and periods of self-similar solution for increasing values of the Reynolds number. Starred values were reported in (Watson et al. 1990).

R	Computed period	Period of self-similar solution
355.5738	–	180*
370	199	199.041
400	248.19	250*
500	445	444.724
600	674.45	674.109
700	934.76	935.161
800	1223.9	1224.2
900	aperiodic	1546.3

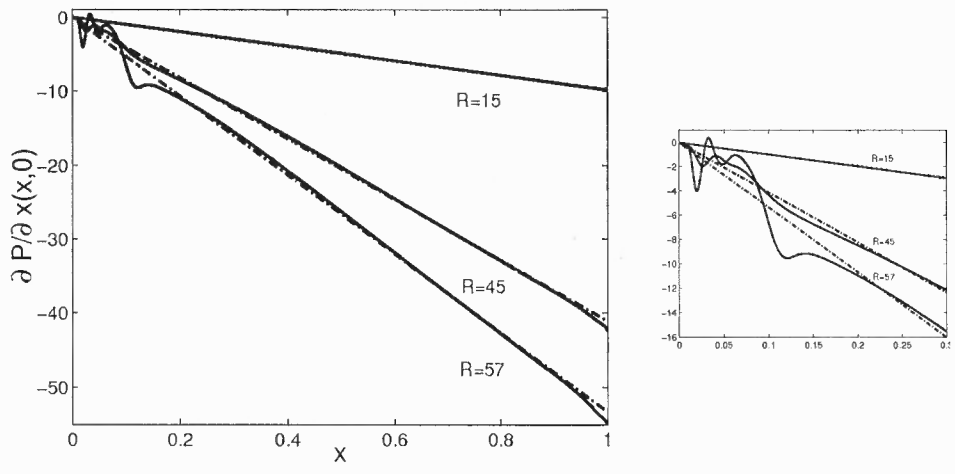

Figure 2.11 Pressure gradients at the channel center line computed from type (II) solutions at different values of the Reynolds number. The dash-dot lines were obtained from the exact solution in the respective cases. At the right we show an enlargement of the region $0 \leq x \leq 0.3$. The aspect ratio of the channel is $\varepsilon = 0.01$

ing the channel collides with the decelerated fluid in the region near $x = 0$ destroying the self-similarity of the solution in this region and affecting the solution in the entire domain. This was confirmed by the linear stability analysis performed in Section 2.4.3. Also, as illustrated by Figure 2.12, where the channel has an aspect ratio of $1/50$, and Figure 2.11 where the aspect ratio is $1/100$, the collision region occupies the same proportion of the domain in terms of the scaled variables.

The development of collision regions when $R > \approx 33$, together with rapidly oscillating edge conditions when the exact solution Hopf bifurcates at $R > 55.77$ results in the

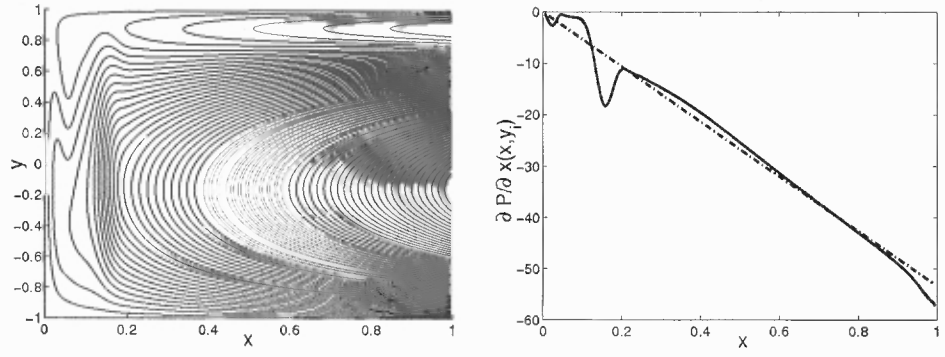

Figure 2.12 Streamlines and pressure gradient at the channel center line computed from type (II) solutions in the case $R = 57$. The dash-dot line was obtained from the exact solution. The aspect ratio of the channel is $\varepsilon = 0.02$

instability of time dependent self-similar flows. As described in Section 2.4.1 rapidly oscillating type (II) conditions can destabilize the flow, producing wave-like structures with length scales of the same order of magnitude of the aspect ratio of the channel, like the ones shown in Figure 2.13. We note that these structures are implicitly neglected when a self-similar solution is assumed to be valid or when scalings where terms of the form $\varepsilon\partial/\partial x$ are assumed to be small.

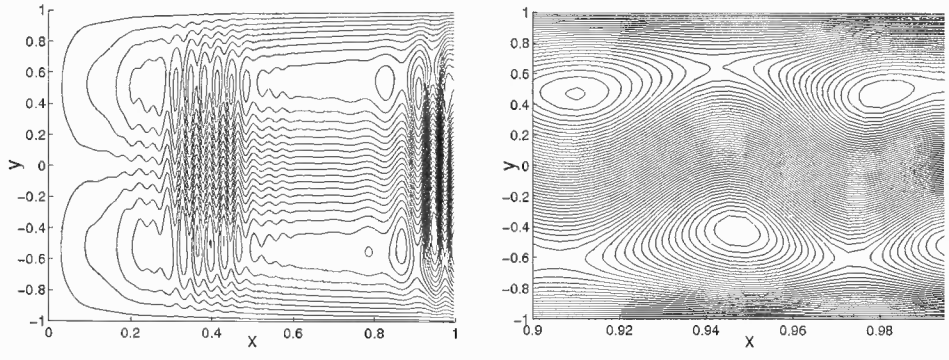

Figure 2.13 Streamlines computed in the case $R = 70$ at time $t = 1014.761$. A time dependent type (II) condition was imposed at $x = 1$. The plot at the right is a enlargement of the region $0.9 < x < 1$. The aspect ratio of the channel is $\varepsilon = 0.01$

2.4.3 Linear Stability of the Similarity Solution f

The fact that we recover type (II) solutions corresponding to stable and unstable branches of the exact solution in the positive Reynolds number case suggest that these branches are

stable for the Navier-Stokes equations. In order to investigate this possibility and also to understand the development of collision regions for Reynolds number below the critical value $R_0 \approx -33$, we performed a linear stability analysis for small perturbations about the exact solution f: if we look for solutions of equations (2.2)-(2.5) of the form

$$u = xf' + \tilde{u} \tag{2.9}$$

$$v = -f + \tilde{v} \tag{2.10}$$

$$p = \frac{\beta}{2}x^2 + p_0 + \tilde{p} \tag{2.11}$$

and we linearize for small $(\tilde{u}, \tilde{v}, \tilde{p})$, we obtain the following equations for the perturbations:

$$\tilde{u}_t + f'(x\tilde{u}_x + \tilde{u}) - f\tilde{u}_y + xf''\tilde{v} = -\frac{1}{R}\tilde{p}_x + \frac{1}{R}(\varepsilon^2\tilde{u}_{xx} + \tilde{u}_{yy}), \tag{2.12}$$

$$\tilde{v}_t + f'(x\tilde{v}_x - \tilde{v}) - f\tilde{v}_y = -\frac{1}{\varepsilon^2 R}\tilde{p}_y + \frac{1}{R}(\varepsilon^2\tilde{v}_{xx} + \tilde{v}_{yy}), \tag{2.13}$$

$$\tilde{u}_x + \tilde{v}_y = 0, \tag{2.14}$$

subject to conditions

$$\begin{aligned} \tilde{u}(0,y) &= 0 \\ \tilde{v}_x(0,y) &= 0 \\ \tilde{u}(x,\pm 1) &= 0 \\ \tilde{v}(x,\pm 1) &= 0 \\ \tilde{u}(1,y) &= u_p(y) \\ \tilde{v}(1,y) &= v_p(y). \end{aligned} \tag{2.15}$$

The functions (u_p, v_p) correspond to perturbations of type (II) conditions at the channel edge which allow us to take into account small perturbations to the profiles used as type (II) conditions at the edge of the domain. The restrictions that u_p and v_p have to satisfy are

$u_p(\pm 1) = v_p(\pm 1) = 0$, and mass conservation in the form

$$\int_{-1}^{1} u_p(y)dy = 0. \tag{2.16}$$

The spatial stability analysis performed by Durlofsky and Brady (1984) provides a useful starting point for our analysis. They studied the evolution of perturbations of the stream function $xf(y)$ of the form $x^{\lambda}g(y)$. This type of perturbation corresponds to the particular case $(\tilde{u}, \tilde{v}) = (x^{\lambda}g', -\lambda x^{\lambda-1}g)$. In the $\varepsilon \to 0$ limit of equations (2.12)-(2.14) perturbations of this form result in the eigenvalue problem

$$g''' + R(fg'' - (\lambda+1)f'g' + \lambda f''g) - (\lambda+1)\gamma = 0, \tag{2.17}$$

subject to conditions

$$\begin{aligned} g(1) = g(-1) &= 0 \\ g'(1) = g'(-1) &= 0 \\ g'''(-1) &= g'''(1), \end{aligned} \tag{2.18}$$

where γ is an unknown parameter. An eigenvalue $\lambda > 1$ implies that perturbations of flows with fluid moving towards zero are stable, and eigenvalues $\lambda < 1$ imply that perturbations of flows with fluid moving towards infinity are stable. It was reported by Durlofsky and Brady (1984) that the symmetric branch of f has only positive eigenvalues for $0 < R < 11$, both positive (larger than one) and negative eigenvalues for $R > 11$ and only negative eigenvalues for negative Reynolds number. They presented two interpretations to these results. In the first one the flow is unstable for all Reynolds numbers since both the accelerating and decelerating wall driven flows have fluid moving towards $x = +\infty$ as well as fluid moving towards $x = 0$. In the second interpretation a distinction is made between fluid in the boundary layers adjacent to the walls which form at larger values of R, and the fluid in the

core which moves in the opposite direction. Under this interpretation the flow is stable for all Reynolds numbers. This ambiguity does not exist in finite channels where perturbations at $x = L$ can only travel to the interior of the channel.

The eigenvalue problem (2.17)-(2.18) can be solved with MATLAB's *bvp4c* package. For a given value of λ and the corresponding eigenfunction g, we define the initial conditions for $(\tilde{u}.\tilde{v})$

$$\tilde{u}_0(x,y) = xg'(y) \tag{2.19}$$

$$\tilde{v}_0(x,y) = -\lambda x g(y) \tag{2.20}$$

which are consistent with the boundary conditions, and we use $(u_p, v_p) = (g', -\lambda g)$ as type (II) conditions at the edge. In Figure 2.14 we show the eigenvalues that we calculated and used in the stability computations shown in Figure 2.15 and the left panel of Figure 2.16. These eigenvalues were obtained by solving equations (2.17)-(2.18) with f in to the asymmetric branch of the exact solution. Since these eigenvalues are negative, we would expect this branch to be spatially unstable to perturbations of the form $(\tilde{u}, \tilde{v}) = (x^\lambda g', -\lambda x^{\lambda-1} g)$ in a finite channel. We will see below that this is not the case. For studying the linear stability of the negative Reynolds number flows we simply construct u_p, v_p and the initial state using polynomials that satisfy the boundary conditions and conservations of mass.

In Figure 2.15 we show the evolution of velocity profiles $\tilde{u}(x, y = 1/2, t)$ for increasing values of t. These profiles were computed with the initial conditions and edge conditions described in the lines above, with g computed for the asymmetric steady branch of f when $R = 357$. The arrows show the direction of the evolution of the profiles. We can clearly see in this Figure that the perturbations introduced at the edge decrease towards zero as the fluid moves away from the edge.

In order to study the evolution of the perturbations in the whole channel we define

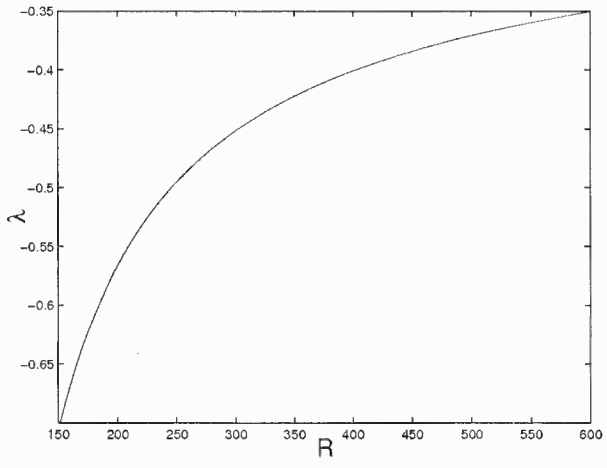

Figure 2.14 Eigenvalues corresponding to the asymmetric branch of the exact solution f.

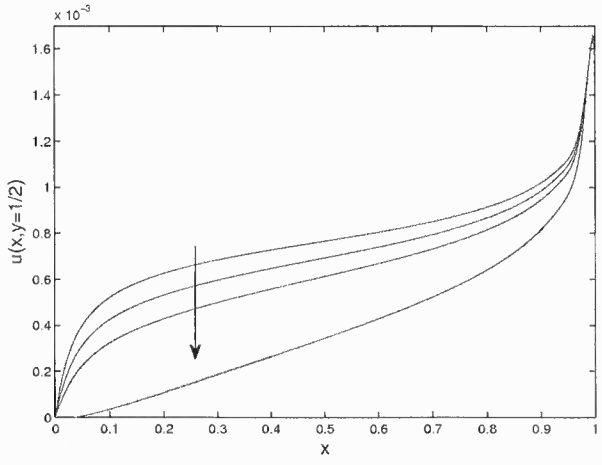

Figure 2.15 Velocity profiles $\tilde{u}(x, y = 1/2)$ at different times, in the case $R = 357$. The arrow shows the direction of increasing time. The aspect ratio of the channel is $\varepsilon = 0.01$.

the integral

$$E(t) = \frac{\int_{-1}^{1}\int_{0}^{1}(\tilde{u}^2 + \tilde{v}^2)dxdy}{\int_{-1}^{1}\int_{0}^{1}(\tilde{u}_0^2 + \tilde{v}_0^2)dxdy}. \tag{2.21}$$

Stable solutions will be characterized by a decreasing $E(t)$ while unstable solutions will have increasing $E(t)$. In Figure 2.16 we show the time evolution of $E(t)$ for perturbations computed at different values of R. This result shows that the asymmetric steady branch of f in the positive Reynolds number case is stable for equations (2.2)-(2.5) in agreement with what was observed in the direct simulations in the respective cases. The final value of $E(t)$ is a positive number because of the non-null perturbations (u_p, v_p) at the channel edge.

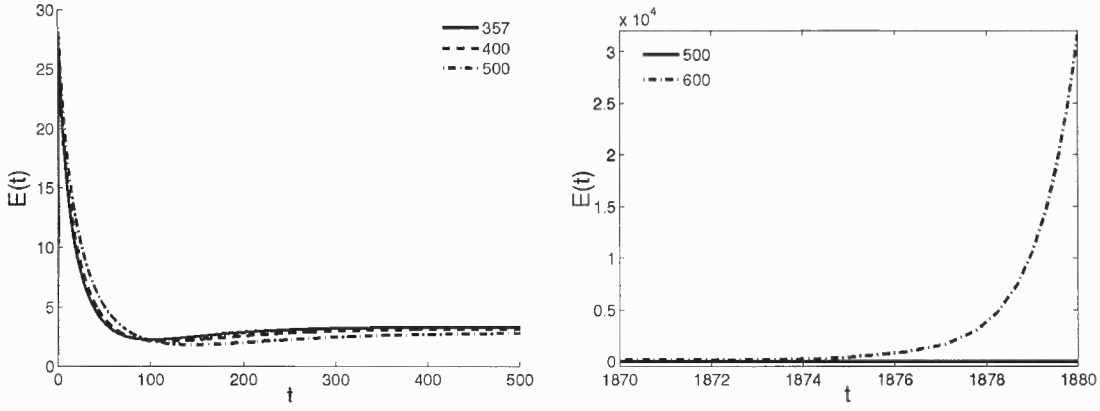

Figure 2.16 Function $E(t)$ computed from solutions at different values of the Reynolds number. Curves in the left panel were computed using solutions of the steady, asymmetric branch and curves in the right panel were computed with time dependent self-similar solutions. The channel aspect ratio is $\varepsilon = 0.01$.

Similar computations can be performed with the symmetric steady branch of f and they show that this branch is stable as well. The resulting Figure has similar characteristics to Figure 2.16 above, and we do not show it here. For completeness, we show stability computations for the time-dependent branch of the similarity solution in the right panel of the same Figure.

In the case of negative Reynolds number we set $(u_p, v_p) = (y^3 - y, 0)$ as edge conditions and we define a initial state by scaling u_p with x between 0 and 1. In Figure 2.17 we show the time evolution of $E(t)$ computed for the values of the Reynolds number shown. As expected from the simulations of Figure 2.11, the case $R = -15$ is stable to spatial perturbations and the cases $R = -45$ and $R = -57$ are unstable to spatial perturbations. A log-log plot of the same quantities showed that $E(t)$ is growing exponentially in the latter two cases. Similar computations performed with the symmetric branch of the self-similar solution show that this solutions are linearly unstable as well, as shown in Figure 2.17.

2.5 Conclusions

We have computed flows in two dimensional channels of finite length L driven by accelerating walls (positive Reynolds number) or by decelerating walls (referred to as negative

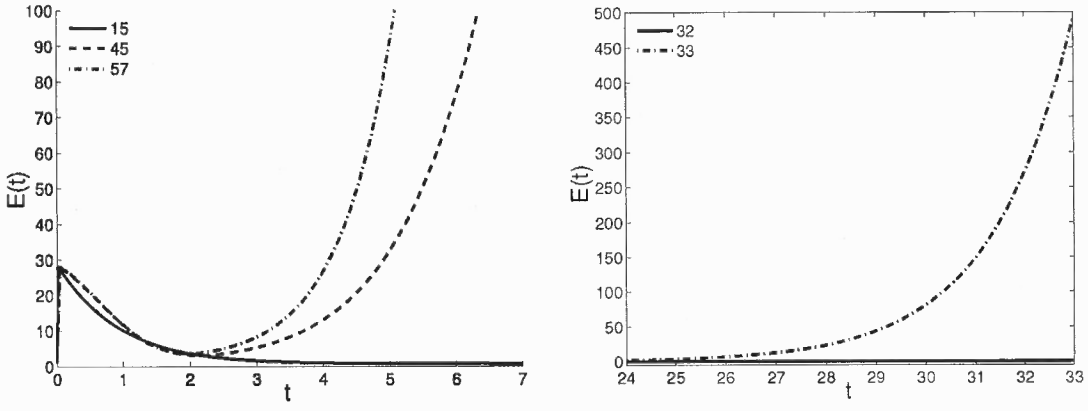

Figure 2.17 Function $E(t)$ computed with solutions of the asymmetric branch (left panel) and the symmetric branch (right panel) of the similarity solution at different values of the Reynolds number. The channel aspect ratio is $\varepsilon = 0.01$.

Reynolds number). The equivalent problems in infinitely long channels admit self similar solutions that can be recovered in a region at the interior of the finite channel which depends on the boundary conditions imposed at the channel end at $x = L$. If the boundary condition does not coincide with the exact solution at $x = L$, the length of the region where the exact solution is recovered decreases with increasing Reynolds number.

For flows driven by accelerating walls, as the Reynolds number increases the self similar solution has a symmetry breaking bifurcation at the value $R = 132.75849$ and a Hopf bifurcation at the value $R = 355.5738$. We showed that stable and unstable steady branches of the self-similar solution are recovered as stable Navier-Stokes flows for values as large as $R = 500$. The stable, time dependent self-similar solutions that exist for values larger than $R = 355.5738$ are recovered as well. The slow time evolution of these time dependent solutions allows the flow to adjust to the changing conditions at the edge of the domain. We note, however, that time dependent solutions can be recovered only if the time dependent exact solution is imposed as boundary condition at $x = L$. If instead, a steady Dirichlet condition is used the flow at the interior of the channel will adjust to this steady condition.

For flows driven by decelerating walls we showed that the self similar solution becomes unstable to spatial perturbations at a critical value $R \approx -33$. For values of the

Reynolds number less than this critical value, the flow develops a collision region at $x = 0$ and within this region the flow is not of self similar form. Time dependent self similar solutions are not found in a finite channel with decelerating walls.

CHAPTER 3

CHANNEL FLOWS DRIVEN BY VERTICALLY OSCILLATING WALLS

In this Chapter, we study flows in infinite or finite two-dimensional channels which are driven by vertical oscillations of their rigid walls. The movement of the walls is prescribed via some periodic function of time, and the symmetry of the domain with respect to one of the spatial variables will allow us to look for self-similar solutions that satisfy a simplified problem, typically a single non-linear partial differential equation. When a finite channel is considered, we will integrate the Navier-Stokes equations numerically, without assuming a special form of the solutions.

3.1 Vertical Oscillations

In this Section we consider flows in a channel whose walls move in the following way: the position of the upper wall is $y = a(t)$ and the position of the lower wall is $y = -a(t)$, as shown in Figure 3.1. The oscillation is given by the function

$$a(t) = a_0(1 + \Delta \cos \omega t), \quad 0 < \Delta < 1. \tag{3.1}$$

We non-dimensionalize the equations of motion (1.1)-(1.3) as follows:

$$x' = \frac{x}{a_0}, \quad y' = \frac{y}{a_0}, \quad t' = \omega_0 t, \quad u' = \frac{u}{\omega_0 a_0}, \quad v' = \frac{v}{\omega_0 a_0}, \quad p' = \frac{p}{\rho a_0^2 \omega_0^2},$$

where $\omega = k\omega_0$, k is a non-dimensional frequency. The non-dimensional equations of

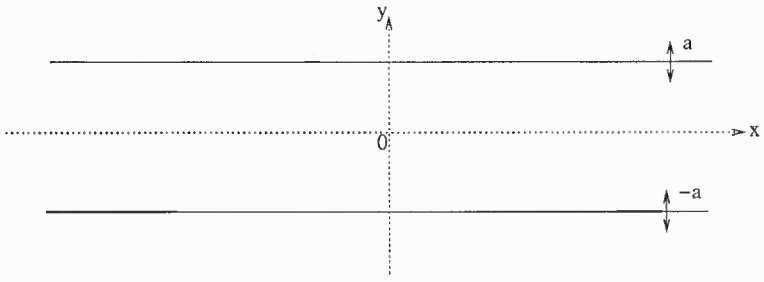

Figure 3.1 Geometry of the problem.

motion are (dropping all primes)

$$u_t + uu_x + vu_y = -p_x + \frac{1}{R}(u_{xx} + u_{yy}), \tag{3.2}$$

$$v_t + uv_x + vv_y = -p_y + \frac{1}{R}(v_{xx} + v_{yy}), \tag{3.3}$$

$$u_x + v_y = 0, \tag{3.4}$$

where $R = \rho\omega_0 a_0^2/\mu$ is the Reynolds number for this flow. Equation (3.1) becomes

$$a(t) = 1 + \Delta\cos kt, \quad 0 < \Delta < 1.$$

Accordingly, the no-slip boundary conditions take the form

$$u = 0,\ v = \pm\dot{a} \quad \text{at} \quad y = \pm a(t). \tag{3.5}$$

The system (3.2)-(3.4) together with boundary conditions (3.5) is characterized by two parameters, the Reynolds number R, and the dimensionless oscillation amplitude Δ. Note that k can be removed from the problem by rescaling time and redefining R. In what follows $k = 2$ so that the forcing $a(t)$ is π periodic. This choice also allows us to compare our results with the ones reported by Hall and Papageorgiou (1999).

Secomb (1978) proposed a solution to equations (3.2)-(3.4) which has the following

form:

$$u = u_0 + xu_1 \tag{3.6}$$

$$v = v(y,t) \tag{3.7}$$

$$p = p_0 + xp_1 + x^2 p_2, \tag{3.8}$$

where u_0, u_1, p_0, p_1, p_2 and the vertical velocity v are functions of t and y alone. This form of the solution results from assuming that the vertical velocity v is independent of x, which is a reasonable simplification in an infinite domain. It follows that u must be linear in x as a consequence of equation (3.4) and that p must be quadratic in x by equation (3.2). It is convenient to 'fix' the walls of the channel by introducing the variable $\eta = y/a$. By substituting equations (3.6)-(3.8) into the equations of motion (3.2)-(3.4) and grouping terms with the same power of x, we obtain the following equations in terms of the new variable η:

$$u_{0t} + u_1 u_0 + (v - \eta\dot{a})\frac{u_{0\eta}}{a} = -p_1 + \frac{1}{Ra^2}u_{0\eta\eta}, \tag{3.9}$$

$$u_{1t} + u_1^2 + (v - \eta\dot{a})\frac{u_{1\eta}}{a} = -2p_2 + \frac{1}{Ra^2}u_{1\eta\eta}, \tag{3.10}$$

$$v_t + (v - \eta\dot{a})\frac{v_\eta}{a} = -\frac{p_{0\eta}}{a} + \frac{1}{Ra^2}v_{\eta\eta} \tag{3.11}$$

$$u_1 + \frac{v_\eta}{a} = 0, \tag{3.12}$$

$$p_{1\eta} = 0, \quad p_{2\eta} = 0, \tag{3.13}$$

$$u_0 = u_1 = 0, \quad v = \pm\dot{a} \text{ at } \eta = \pm 1. \tag{3.14}$$

Equations (3.10)-(3.11) for u_1, v and p_2 can be solved independently of equation (3.9) for u_0 and p_1. As a consequence of equation (3.12), we can define a *stream function* for u_1 and v, and reduce the system (3.10)-(3.12) to a single partial differential equation; see Section 3.2.1. Once the equation for the stream function is solved we can compute p_2 and p_0 from equations (3.10) and (3.11) respectively. The unknown p_1 is only restricted by

equation (3.13) and the remaining, linear equation (3.9) for the longitudinal flow u_0 can be solved if the pressure gradient p_1 is prescribed. In Section 3.2 we study the flow u_0 in the case when $p_1(t)$ is constant.

3.2 Dynamics of the Horizontal Flow u_0

In this Section we study the dynamics of the horizontal flow u_0, which is governed by equation (3.9). For simplicity we consider the case when the pressure gradient $p_1(t)$ is constant and $O(1)$. Equation (3.12) implies that there is a scalar function $\Psi = xf(\eta,t)$ which satisfies

$$u_1 = \frac{1}{a} f_\eta, \tag{3.15}$$

$$v = -f, \tag{3.16}$$

(see Spivak (Spivak 1965)). Thus, by rescaling equation (3.9) with the constant p_1 and replacing u_1 and v with the expressions above we obtain (dropping the primes of all the rescaled quantities)

$$u_{0t} = -1 - \frac{f_\eta}{a} u_0 + (f + \eta \dot{a}) \frac{u_{0\eta}}{a} + \frac{1}{Ra^2} u_{0\eta\eta}, \quad u_0(\pm 1, t) = 0. \tag{3.17}$$

A brief description of the main results regarding f is given in Section 3.2.1 below. In Section 3.2.2 we discuss the properties of the flow u_0 valid in the small Reynolds number regime and in Section 3.3 we discuss the bifurcations of (3.17) which occur at higher values of R.

3.2.1 Stagnation Point Flow

By differentiating equation (3.10) with respect to η and replacing u_1 and v with expressions (3.15) and (3.16) we obtain the one-dimensional partial differential equation

$$f_{\eta\eta t} = \frac{\dot{a}}{a}(2f_{\eta\eta} + \eta f_{\eta\eta\eta}) + \frac{1}{Ra^2} f_{\eta\eta\eta\eta} + \frac{1}{a}(f f_{\eta\eta\eta} - f_\eta f_{\eta\eta}), \tag{3.18}$$

which is subject to boundary conditions

$$f_\eta(\pm 1, t) = 0, \tag{3.19}$$

$$f(\pm 1, t) = \mp \dot{a}. \tag{3.20}$$

This equation has been studied in detail by Hall and Papageorgiou (1999). For any fixed value of the oscillation amplitude Δ, the flow is synchronous with the wall oscillation $a(t)$ and symmetric about $\eta = 0$ for small values of the Reynolds number. If R increases there is a symmetry breaking bifurcation, and if R is increased further the flow becomes chaotic. The chaotic state is the result of a period doubling cascade or a quasi-periodic flow, depending on the value of Δ. Also, it is important to mention that the flow driven by decelerating walls studied in Chapter 2 appears as a core flow driven by the steady forcing generated by the wall layers in the small oscillation amplitude – large Reynolds number limit of the flow f. For details about these results, see (Hall and Papageorgiou 1999).

3.2.2 Solution for Small Reynolds Number

When R is small, we can solve equations (3.9)-(3.14) by using a regular asymptotic expansion of the unknowns in powers of R. Let

$$u_1 = u_{10} + Ru_{11} + O(R^2)$$
$$v = v_0 + Rv_1 + O(R^2)$$
$$u_0 = u_{00} + Ru_{01} + O(R^2).$$

We can eliminate the pressure term from equation (3.10) by differentiating it with respect to η. Then by equation (3.12), we find that the leading order terms in the expansion for u_1 and v that satisfy the boundary conditions (3.14) are

$$v_0 = \frac{\dot{a}}{2}(3\eta - \eta^3), \tag{3.21}$$
$$u_{10} = \frac{3}{2}\frac{\dot{a}}{a}(\eta^2 - 1). \tag{3.22}$$

These are seen to be a squeeze flow and a Poiseuille flow. To find the leading order term in the expansion for u_0 we assume that the prescribed pressure gradient p_1 is constant. As a consequence of the homogeneous boundary conditions the first term in the expansion, u_{00}, is zero. The first non-null term in the expansion is u_{01}:

$$u_{01} = \frac{p_1 a^2}{2}(\eta^2 - 1). \tag{3.23}$$

If we keep calculating the higher order terms in the expansion for u_0 we find that all of them are even polynomials in the variable η.

3.3 Bifurcations of the Horizontal Flow u_0 at Higher Values of R

For $O(1)$ values of the Reynolds number, we solve equation (3.17) numerically. The details of the numerical scheme we employ are given in Appendix C. In the present case

$$a = 1 + \Delta \cos 2t, \quad 0 < \Delta < 1, \tag{3.24}$$

and, as discussed in the previous Section, the pressure driven flow u_0 is symmetric around $\eta = 0$, as well as periodic with the same period as $a(t)$ for small values of the Reynolds number. As described previously, the background flow f loses symmetry at a bifurcation value of R which is a function of Δ. It is natural to expect a similar behavior for u_0 as it depends explicitly on f. However, the set of bifurcations of u_0 is surprisingly complex as evidenced by Figure 3.2:

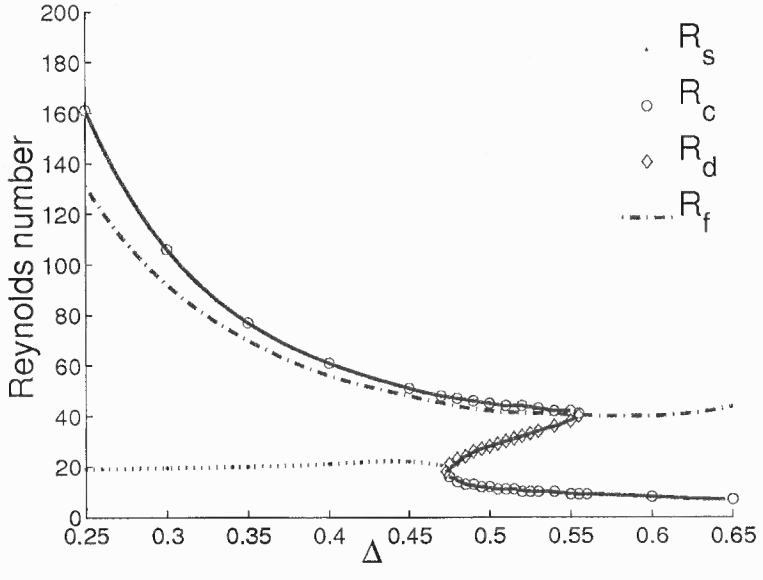

Figure 3.2 Bifurcation diagram for the flow u_0.

The dash-dot line in Figure 3.2 indicates the location, in the parameter space Δ-R, where the symmetry breaking bifurcation of f occurs (values taken from (Hall and Papageorgiou 1999)). The dotted line shows the location of symmetry breaking bifurcation of u_0 and the solid line shows the location of the change of stability of u_0. In the region

'below' the solid line the flow is time periodic and in the region 'above' the solid line the flow is growing exponentially in time. Likewise, above the dotted line u_0 is asymmetric and below it, u_0 is an even function of η. Points in the doted line are labeled R_s, the meaning of the other symbols in Figure 3.2 and a detailed characterization of the different states of the flow are given in Section 3.3.

In order to quantify a symmetry breaking bifurcation we consider the function ηu_0^2, which is an odd function of η provided that u_0 is symmetric around $\eta = 0$. The integral

$$I(R,\Delta) = \sqrt{\frac{|\int_{t_0}^{t_0+\pi}\int_{-1}^{1}\eta u_0^2 d\eta dt|}{\int_{t_0}^{t_0+\pi}\int_{-1}^{1}u_0^2 d\eta dt}}, \tag{3.25}$$

indicates any change in the symmetry properties of u_0; for example, I is zero as long as u_0 remains even. It is understood that t_0 is large enough so that any transients in the solution disappear and a periodic state is attained, for example we took $t_0 = 700\pi$. At time $t = 0$ we set $u_0 = 0$ and march forward in time until a periodic state is reached. Note that we have normalized the value of the integral in order to control its size. For small values of R and for any value of Δ the value of $I(R,\Delta)$ is zero, as expected. The solution is bounded and time-periodic of period π. As R increases the amplitude of the oscillations is also found to increase. This behavior remains unaltered for a range of values of R until a critical value R_s is reached, above which the solution is no longer symmetric. This can be seen in Figure 3.3, where we show $I(R,\Delta = 0.35)$. At $R_s \approx 20$ there is a pitchfork bifurcation to a solution with $I \neq 0$. Solutions in the other stable branch can be computed by reflection about $\eta = 0$ combined with standard continuation techniques in the Reynolds number. As can be seen in Figure 3.2, u_0 losses symmetry at values of R which are much smaller than the corresponding values for f.

In the region $0.473 \lesssim \Delta \lesssim 0.556$ three bifurcations occur. For any fixed Δ within this region the flow changes it stability properties when R crosses the solid line shown in Figure 3.2. For example, when $\Delta = 0.5$, if $R \lesssim 12$ (labeled as R_c), the flow is stable, if

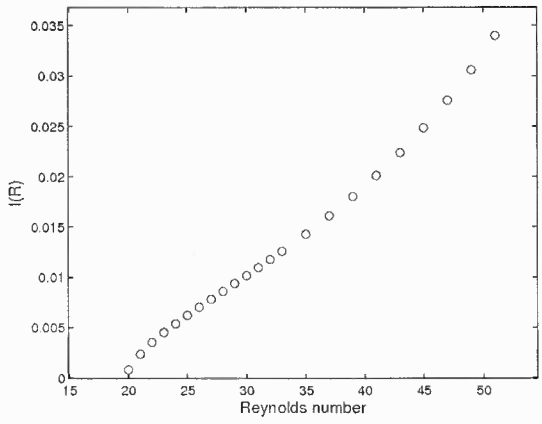

Figure 3.3 Values of $I(R)$ for $\Delta = 0.35$.

$R \lesssim 28.03$ (labeled as R_d) but larger than 12 the flow is unstable and if $R \lesssim 45$ (labeled as R_c) but larger than 28.03 the flow is stable. For values of R larger than 45, the flow is unstable again. For values of Δ outside the region $0.473 \lesssim \Delta \lesssim 0.556$ the flow becomes unstable when R is above the solid line in Figure 3.2.

In Figures 3.4, 3.5 and 3.6 we show velocity profiles for the case $\Delta = 0.35$, which are characteristic of the different regimes of the flow u_0: symmetric state, asymmetric and stable state, and growing exponentially in time.

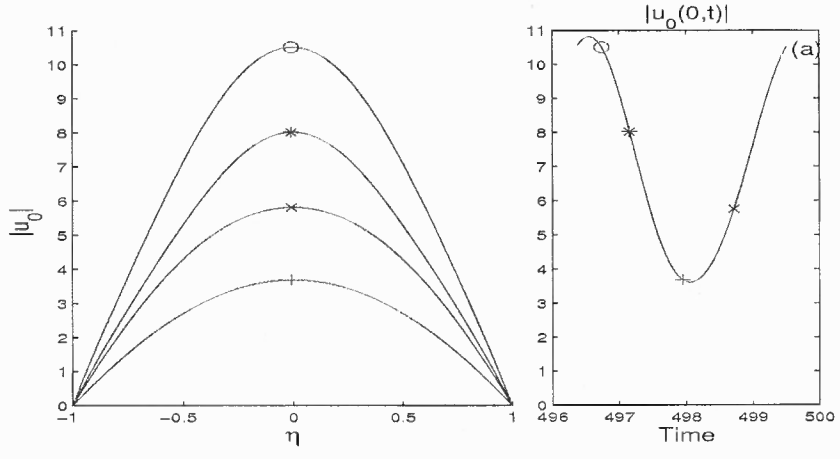

Figure 3.4 Velocity profiles in the case $\Delta = 0.35$ and $R = 10$ ($R < R_s$).

When $\Delta = 0.35$, the critical value R_c satisfies $77 < R_c < 78$. To illustrate this we show in Figure 3.7 the signal defined by $s(t) = u_0(-1/2, t)$ when $R = 77$ and the logarithm

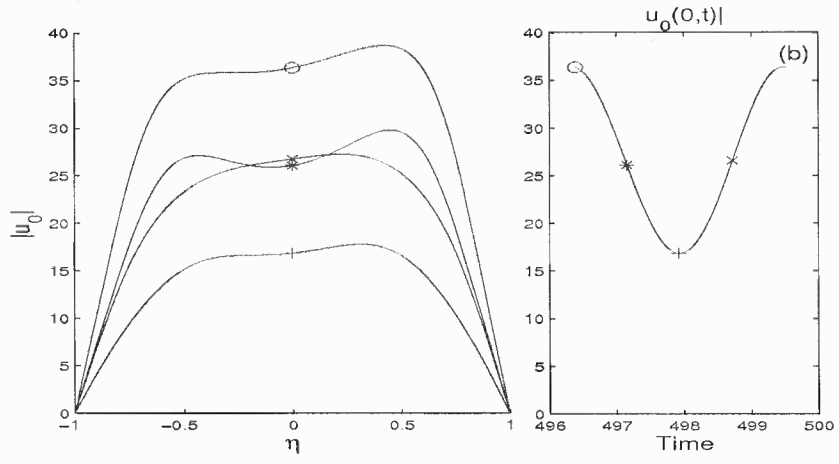

Figure 3.5 Velocity profiles in the case $\Delta = 0.35$ and $R = 70$ $(R_s < R < R_c)$.

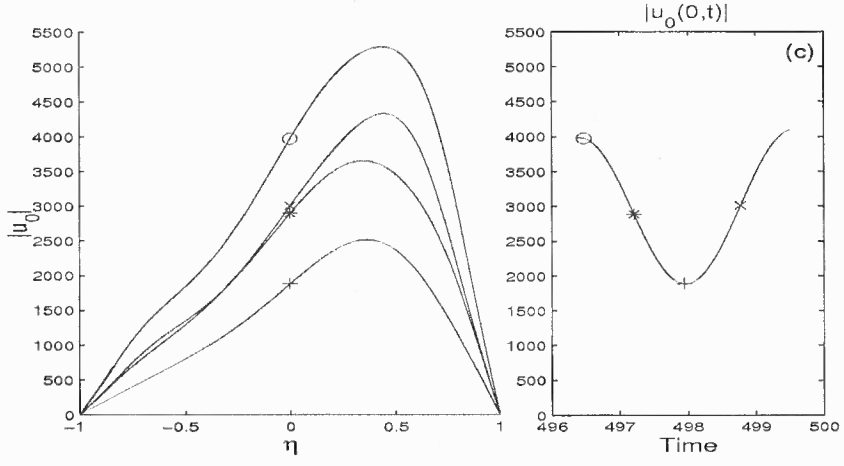

Figure 3.6 Velocity profiles in the case $\Delta = 0.35$ and $R = 80$ $(R_c < R)$.

of the corresponding signal in the case $R = 78$ which demonstrates the exponential growth of the function $s(t)$:

Floquet theory provides a basis in which the changes of stability of the pressure driven flow u_0 that occur at the values R_c and R_d can be understood. Equation (3.23), which governs u_0, is linear and we can decompose this flow in two parts, one that is driven by the pressure gradient p_1 and another one that is driven by the oscillations of the wall alone:

$$u_0 = u_p + \hat{u}, \tag{3.26}$$

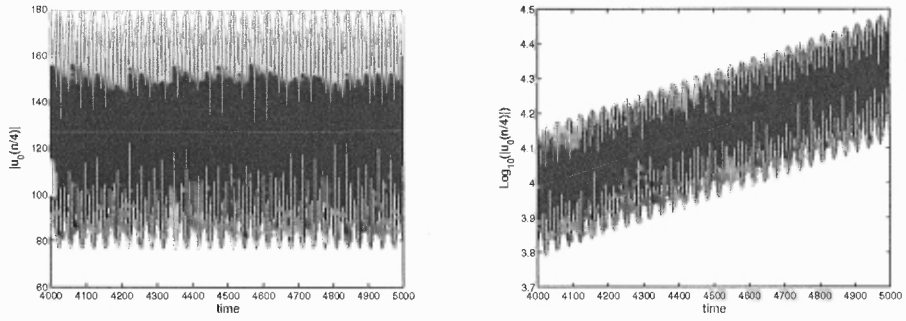

Figure 3.7 Signal $s(t)$ for $\Delta = 0.35$ and (a) $R = 77$, (b) $R = 78$. The white lines result from the linear interpolation of the signal and the logarithm of the signal, respectively.

with $\hat{u}$ satisfying the equation

$$\hat{u}_t = -\frac{f_\eta}{a}\hat{u} + (f + \eta\dot{a})\frac{\hat{u}_\eta}{a} + \frac{1}{Ra^2}\hat{u}_{\eta\eta}, \tag{3.27}$$

and boundary conditions $\hat{u}(\pm 1,t) = 0$. For the values of R considered, all the coefficients in the linear partial differential equation (3.27) remain time periodic. Formally, we expect that $\hat{u}$ can be written in the form

$$\hat{u} = e^{\mu(\eta)t}U(\eta,t), \quad U(\eta,t+\pi) = U(\eta,t).$$

For any fixed η, the value $\mu(\eta)$ can be estimated from the signal $s(t) = \hat{u}(\eta,t)$, once the initial boundary value problem for $\hat{u}$ is solved (we use an arbitrary, non-zero initial condition). In this context, the bifurcations that occur at $R = R_c$ correspond to a transcritical bifurcation. As μ crosses from the negative real axis to the positive real axis (we found numerically that μ is real) an exchange of stability of the equilibrium of equation (3.27) occurs. In the case of R_d, μ crosses from the positive real axis to the negative real axis.

In the region 'above' the solid line shown in Figure 3.2, the Floquet exponent is positive and a monotonically increasing function of R, as can be seen for example, in Figure 3.8 for the particular case $\Delta = 0.35$. We carried out calculations for values of R as large as a thousand, for several value of Δ, and we did not find any further changes in this behavior

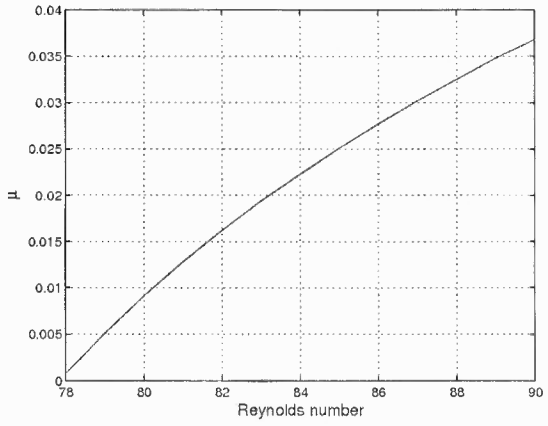

Figure 3.8 Floquet exponent as a function of R. $\Delta = 0.35$.

of the flow u_0.

3.4 A Squeezing, Stretching Channel

In this Section we consider a stagnation point flow which describes a more general problem that the one studied in Section 3.1. However, as we will see, this self-similar flow is still governed by equation (3.18) subject to modified boundary conditions.

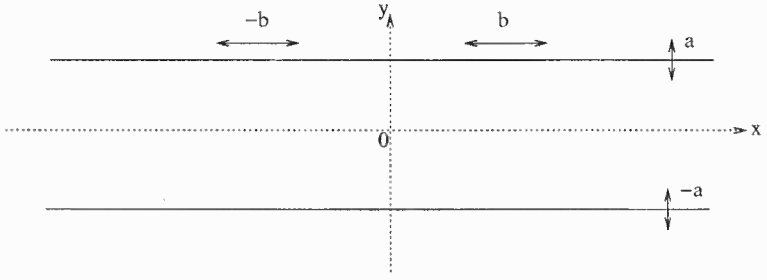

Figure 3.9 Geometry of the problem.

Consider a channel whose walls oscillate in the following way: the position of the walls is $y = \pm a(t)$ and $x = b(t)\bar{x}$, where $\bar{x} = x(0)$ is the initial horizontal position of the

wall. The functions a and b are given by $a = a_0 a'$ and $b = a_0 b'$ where

$$a' = 1 + \Delta_1 \sin(\omega t), \tag{3.28}$$

$$b' = 1 + \Delta_2 \sin(\omega t + q_0). \tag{3.29}$$

The non-dimensional constants $0 < \Delta_1, \Delta_2 < 1$ are the oscillation amplitudes and q_0 is a phase shift. As in the previous example, it is convenient to change to a frame of reference where the channel walls are fixed. Accordingly we non-dimensionalize the Navier-Stokes equations (1.1)-(1.3) in the following way

$$\xi = \frac{x}{a_0 b'}, \quad \eta = \frac{y}{a_0 a'}, \quad t' = \omega t, \quad u' = \frac{u}{\omega a_0}, \quad v' = \frac{v}{\omega a_0}, \quad p' = \frac{p}{\rho a_0^2 \omega^2}.$$

Then the non-dimensional equations are (dropping all the primes)

$$u_t - \xi \frac{\dot{b}}{b} u_\xi - \eta \frac{\dot{a}}{a} u_\eta + \frac{1}{b} u u_\xi + \frac{1}{a} v u_\eta = -\frac{1}{b} p_\xi + \frac{1}{R}\left(\frac{1}{b^2} u_{\xi\xi} + \frac{1}{a^2} u_{\eta\eta}\right), \tag{3.30}$$

$$v_t - \xi \frac{\dot{b}}{b} v_\xi - \eta \frac{\dot{a}}{a} v_\eta + \frac{1}{b} u v_\xi + \frac{1}{a} v v_\eta = -\frac{1}{a} p_\eta + \frac{1}{R}\left(\frac{1}{b^2} v_{\xi\xi} + \frac{1}{a^2} v_{\eta\eta}\right), \tag{3.31}$$

$$\frac{1}{b} u_\xi + \frac{1}{a} v_\eta = 0, \tag{3.32}$$

where again $R = \rho \omega a_0^2 / \mu$. The non-slip boundary conditions in this case are

$$u(\xi, \pm 1, t) = \dot{b}\xi, \quad v(\xi, \pm 1, t) = \pm \dot{a}, \tag{3.33}$$

with a, b given by (3.28)-(3.29), primes removed.

We can modify the ansatz (3.6)-(3.8) to take into account the horizontal oscillations

by making the following modifications:

$$u = \xi b U, \tag{3.34}$$

$$v = -V, \tag{3.35}$$

$$p = \xi^2 b^2 P + P_0, \tag{3.36}$$

where the unknowns U, V, P and P_0 are independent of ξ. Note that we have not included the terms that correspond to u_0 and p_1 in the previous problem, because we are not interested in considering the effects of a driving horizontal pressure gradient, at least at this stage. This effect can be included in a straightforward way by including u_0 and p_1 in the ansatz. The minus sign in front of (3.35) was included for convenience, as it was done with equation (3.16).

We substitute these equations into (3.30)-(3.32), and replace $U = V_\eta / a$ in the momentum equation (3.30) to find that V satisfies

$$V_{\eta\eta t} = \frac{\dot{a}}{a}(2V_{\eta\eta} + \eta V_{\eta\eta\eta}) + \frac{1}{Ra^2} V_{\eta\eta\eta\eta} + \frac{1}{a}(V V_{\eta\eta\eta} - V_\eta V_{\eta\eta}), \tag{3.37}$$

subject to boundary conditions

$$V(\pm 1, t) = \mp \dot{a} \tag{3.38}$$

$$V_\eta(\pm 1, t) = \frac{a\dot{b}}{b}, \tag{3.39}$$

where $a = 1 + \Delta_1 \sin(t)$, $b = 1 + \Delta_2 \sin(t + q_0)$. Is now clear from equation (3.39) that as the amplitude of the horizontal oscillations go to zero we recover the flow (3.18)-(3.20).

In the following Section we briefly discuss some of the characteristics of the self-similar flow defined by V, with special emphasis on the states that occur at moderate oscillation amplitudes ($\Delta_1 = \Delta_2 \leq 0.4$) and moderately large values of the Reynolds number ($R \leq 150$). This flow is part of a model for oxygen transport and diffusion, which we study

in Chapter 4 and the regime that we just described is important for that application of this flow. As described in (Hall and Papageorgiou 1999), flows governed by equation (3.37) support very complex dynamics and have rich sets of bifurcations and bifurcated states (see Section 3.2.1). It is outside the scope of the present study to provide a comprehensive classification of such states; we will only show particular examples of cases in the four-dimensional parameter space $\Delta_1 - \Delta_2 - q_0 - R$ and we will describe a very interesting effect of the phase parameter q_0 which can completely "laminarize" flows which are otherwise chaotic, for example.

3.5 The Effects of Wall Stretching

We find numerically that for small values of the Reynolds number and any value of the oscillation amplitudes the flow is synchronous with the wall motion. This behavior is characteristic for these types of flows, and an example is the flow (3.18)-(3.20) which is recovered in the $\Delta_2 = 0$ limit.

First we consider the case $\Delta_1 = \Delta_2 = 0.4$, $q_0 = 0$ and we track the changes that occur to the flow as R grows. As described in Section 3.3, a quantity like the integral defined in equation (3.25) can be used to characterize a symmetry breaking bifurcation which in the present case occurs at the value $R \approx 39$. In order to analyze the dynamics of the flow at larger values of R, we construct a time signal by $V_0(t) = V(-1/2,t)$. When the flow is synchronous with the wall motion this signal is a 2π-periodic function of time, all its maxima are equal and separated by a period of 2π. If we denote the maxima of the signal by $\{M_i\}$ and the times when a maximum M_i is attained by t_i, it follows that in this case these points satisfy $M_{i+1} = M_i$ and $t_{i+1} - t_i = 2\pi$, $i = 1,2,\ldots$. We can use these values to construct a Poincaré return map by plotting the points (M_i, M_{i+1}), $i = 1,2,\ldots$. Clearly, the return map of a 2π periodic signal consists of a single point. When a period doubling bifurcation occurs, the maxima of the signal lie in two straight lines with its points satisfying $M_{i+2} = M_i$, $t_{i+2} - t_i = 4\pi$, $i = 1,2,\ldots$ and the return map consists of two points

(see Figure 3.10 for an example). Subsequent period doubling bifurcations appear in the maxima plots as an increasing number of straight lines (4, 8 etc). If a signal is quasi-periodic its return map will appear as a filled curve or several of these continuous looking lines. The appearance of foldings and self-similarity in the return map are indicators of chaotic flow. More details about these methods and their use in studying time series can be obtained from Bergé et al. (1984) and examples of the use of velocity signals in classifying flow dynamics are presented in (Hall and Papageorgiou 1999) and (Blyth et al. 2003).

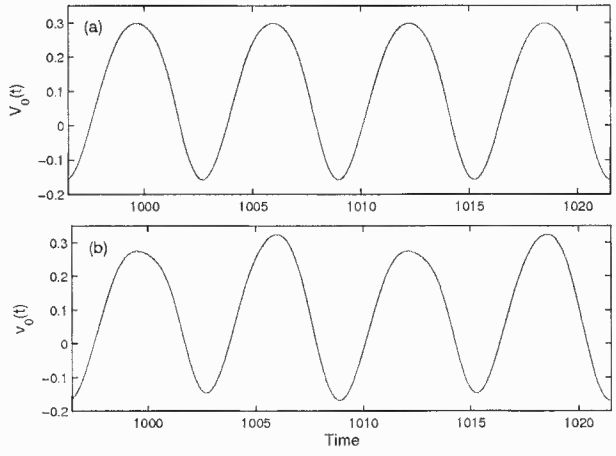

Figure 3.10 Velocity signal $V_0(t)$ in the cases $\Delta_1 = \Delta_2 = 0.4$, $q_0 = 0$ and (a) $R = 130$, (b) $R = 135$.

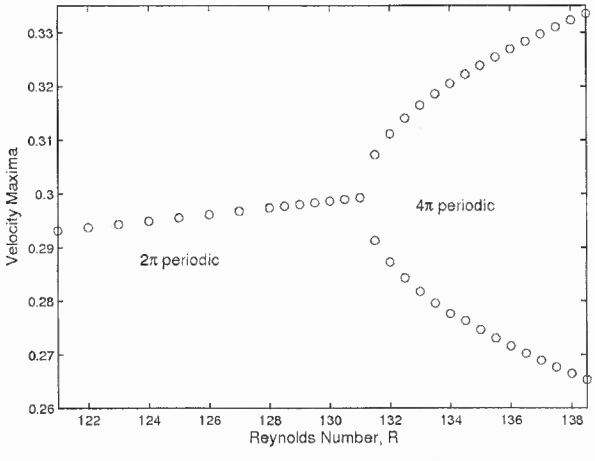

Figure 3.11 Velocity maxima as function of R in the case $\Delta_1 = \Delta_2 = 0.4$, $q_0 = 0$.

In Figure 3.11 we show the maxima of the signal $V_0(t)$ versus R; we estimate the

maxima of the signal by doing a quadratic polynomial interpolation when a change in monotonicity of the curve $V_0(t)$ is detected. Initially the flow is 2π periodic in time and this behavior remains unaltered until the value $R \sim 131$. At this value a period doubling bifurcation to a 4π periodic signal occurs. The signals remain 4π-periodic for a range of values, until $R \sim 151$ is attained, when a new period doubling occurs. The signal remains 8π periodic until the value $R \sim 154$ where the maxima of $V_0(t)$ appear not to follow a distinguished pattern anymore (see Figure 3.13). Foldings in the return map and a dense spectrum (see Figure 3.12) are indicators of a chaotic flow. The same behavior is characteristic for the signals obtained at larger values of R (the largest value of R for which we did computations is $R = 360$).

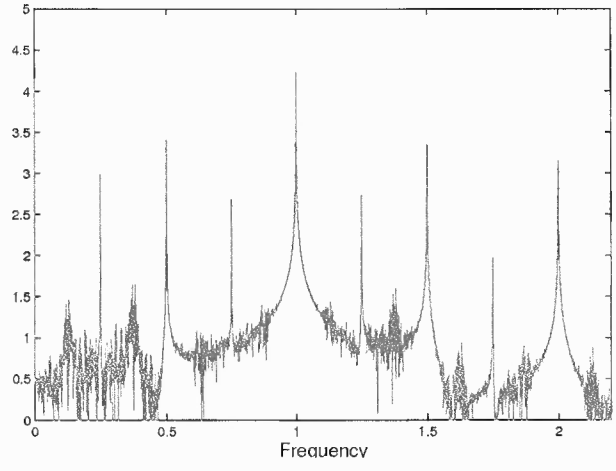

Figure 3.12 Spectrum of the velocity signal $V_0(t)$ in the case $\Delta_1 = \Delta_2 = 0.4$, $R = 154$, $q_0 = 0$.

Until now we have not considered the effect of the phase q_0 on the solutions. So far the most interesting effect that we observed is that of "stabilization" or "laminarization"of the flow by setting the wall oscillations completely out of phase. By setting $q_0 = \pi/2$ and keeping all the other parameters unchanged, we observed that any flow changed to a basic 2π-periodic state. We confirmed this in many different cases including some where chaotic states were found for the in-phase oscillating walls. A connection between a given state occurring with in-phase oscillations and the return to the basic 2π-periodic state via small

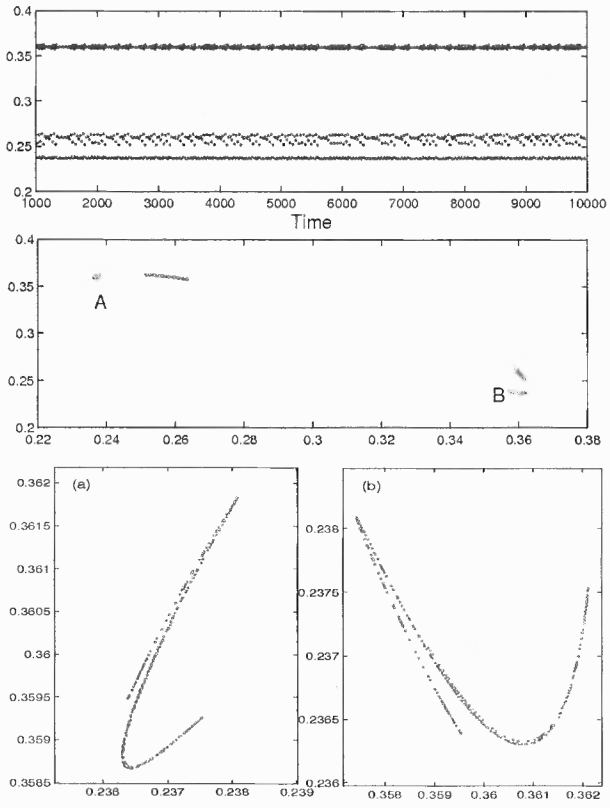

Figure 3.13 Velocity maxima as function of time and Poincaré map for the case $\Delta_1 = \Delta_2 = 0.4$, $R = 154$, $q_0 = 0$. Enlargements of the regions near A and B are shown in (a), (b), respectively.

increments in the phase parameter from 0 to $\pi/2$ could be the part of a future investigation.

3.6 Oscillating Flows in Finite Domains

In this Section we address the question of how the self-similar flows that we have studied in this Chapter behave when the fluid domain is truncated to a channel of finite length. We know from the literature (Hewitt and Hazel (2007), Brady and Acrivos (1982*a*)) and by the results of Section 2.3 concerning type (I) boundary conditions that non-linear modifications to a self-similar solution at the edge of a finite domain will result in an *adaptation region* which grows in length with increasing Reynolds number, and within this region the flow looses self-similarity. Eventually, when R is large enough, the adaptation region occupies the whole domain. For steady flows, this happens at moderately large values of R. We an-

ticipate that the unsteadiness of flows driven by oscillatory walls will affect the stability of any self-similar solution at smaller values of the Reynolds number. As observed in Section 2.4, in the case of flows driven by accelerating walls, unsteady branches become linearly unstable at some finite albeit large value of R. In this Section we concentrate in finding approximate ranges of values of $R(\Delta)$ for which the self-similar solution is recovered as a Navier-stokes flow, when we impose self-similar profiles as Dirichlet conditions at the edge of the domain (what we called type (II) conditions in Section 2.3).

The oscillating channel of this Section has finite length $b(t) = b_0 b'$ and half width $a(t) = a_0 a'$ where a' and b' are time-periodic functions. We use a *viscous scaling* and non-dimensionalize the dependent and independent variables as follows

$$\xi = \frac{x}{b_0 b'}, \quad \eta = \frac{y}{a_0 a'}, \quad t' = \omega t, \quad u' = \frac{u}{\omega b_0}, \quad v' = \frac{v}{\omega a_0}, \quad p' = \frac{a_0^2 p}{b_0^2 \omega \mu},$$

which results in the following dimensionless equations (primes dropped)

$$u_t - \xi \frac{\dot{b}}{b} u_\xi - \eta \frac{\dot{a}}{a} u_\eta + \frac{1}{b} u u_\xi + \frac{1}{a} v u_\eta = -\frac{1}{Rb} p_\xi + \frac{1}{R}\left(\frac{\delta^2}{b^2} u_{\xi\xi} + \frac{1}{a^2} u_{\eta\eta}\right), \tag{3.40}$$

$$v_t - \xi \frac{\dot{b}}{b} v_\xi - \eta \frac{\dot{a}}{a} v_\eta + \frac{1}{b} u v_\xi + \frac{1}{a} v v_\eta = -\frac{1}{\delta^2 Ra} p_\eta + \frac{1}{R}\left(\frac{\delta^2}{b^2} v_{\xi\xi} + \frac{1}{a^2} v_{\eta\eta}\right), \tag{3.41}$$

$$\frac{1}{b} u_\xi + \frac{1}{a} v_\eta = 0, \tag{3.42}$$

where $R = \rho \omega a_0^2 / \mu$, as in Section 3.4. We will be mostly computing flows in slender channels, satisfying $\delta = a_0/b_0 \ll 1$. We need a set of four boundary conditions to complete the system. For compatibility with stagnation point similarity flows we impose symmetry at $\xi = 0$

$$u(0,\eta,t) = 0, \tag{3.43}$$

$$v_\xi(0,\eta,t) = 0. \tag{3.44}$$

The no-slip boundary conditions at the top and bottom walls are

$$u(\xi,\pm 1,t)=\dot{b}\xi, \quad v(\xi,\pm 1,t)=\pm\dot{a}. \tag{3.45}$$

At the channel entrance at $\xi=1$ we impose the Dirichlet condition

$$u(1,\eta,t)=\frac{b}{a}V_\eta(\eta,t), \tag{3.46}$$

$$v(1,\eta,t)=-V(\eta,t), \tag{3.47}$$

where V satisfies equation (3.37) subject to (3.39). Conditions (3.46)-(3.47) correspond to what we called type (II) conditions in Section 2.3. The numerical method described in that Section can be modified to solve equations (3.41)-(3.47). The problem for V is solved numerically with the solver described in (Hall and Papageorgiou 1999) and the flow V is coupled to the modified Navier-Stokes solver of Section 2.3 through equations (3.46)-(3.47).

Considering that all the stagnation point self-similar flows of this Chapter are governed by the same basic equation (3.18), and that cases corresponding to different forcings at the walls can be obtained via elementary transformations, we consider only the case of vertically oscillating channels:

$$a=1+\Delta\cos(2t), \tag{3.48}$$

$$b=1, \tag{3.49}$$

and we adjust the boundary conditions for the Navier-Stokes flow accordingly. Also, it is important to note that we have abundant knowledge about the self-similar solution driven by oscillations (3.48)-(3.49) thanks to the detailed study of Hall and Papageorgiou (1999). For all the computations performed in this Section we set the aspect ratio of the channel to be $\delta=0.01$.

First we analyze the case $\Delta = 0.45$ in some detail. For this value of the amplitude, as R increases the flow V has a symmetry breaking bifurcation at the value $R \approx 44$. In Figure 3.14 we show approximately 150 superimposed Navier-Stokes velocity profiles $u(\xi_i, \eta)/\xi_i$, with ξ_i in the interval [0.035156 0.58203] at time $t = 65.4096$. These profiles were computed in the case $\Delta = 0.45$ and $R = 10$. The dash-dot line represents the self-similar profile imposed as type (II) condition at $\xi = 1$. In the right panel we show velocity signals $s(t) = u(1/2, 0, t)/(1/2)$ computed in the same case $\Delta = 0.45$, $R = 10$ from the Navier-Stokes (solid) and self-similar (dash-dot) flows. Since the self-similar solution prescribed at the edge of the domain changes with time, this information has to travel to the interior producing a delay which is shown in Figure 3.14 as a discrepancy between the interior self-similar profiles and the self-similar solution. As can be seen from the signals, the discrepancy shown in the left panel is nearly the worst case, and for about half of each period both flows are indistinguishable. In the left panel of Figure 3.15 we show the streamlines of the Navier-Stokes flow computed at time $t = 65.4096$ to show the smooth transition between the interior self-similar profiles and the type (II) condition imposed at $\xi = 1$.

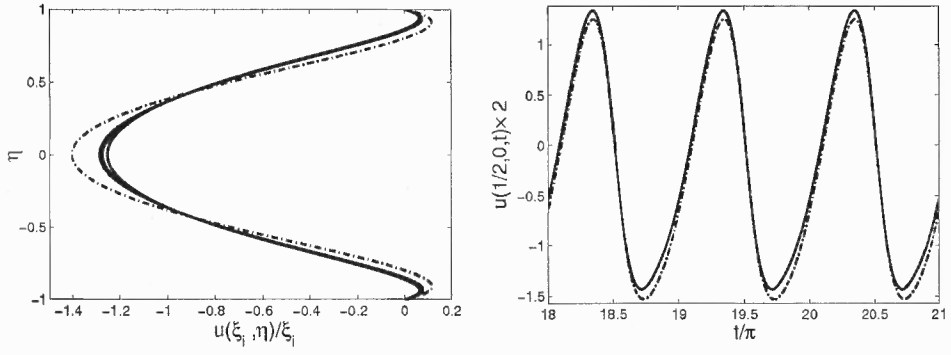

Figure 3.14 Velocity profiles $u(\xi_i, \eta)/\xi_i$, in the range $0.035156 \leq \xi_i \leq 0.58203$ at time $t = 20.8205\pi$ in the case $\Delta = 0.45$ and $R = 10$. The dash-dot line is the self-similar type (II) condition imposed at $\xi = 1$. In the right panel we show the corresponding velocity signals $2 \times u(1/2, 0, t)$. Solid line, Navier-stokes computations. Dash-dot line, self-similar solution. The aspect ratio of the channel is $\delta = 0.01$.

To illustrate the time evolution of the solutions in the entire domain we show the

kinetic energies of the Navier-stokes flow (solid line) and self-similar solution (dash-dot line) in the right panel of Figure 3.15. The Navier-Stokes solution is indistinguishable from the self-similar solution during most of each period and the time ranges where there are discrepancies between the two curves correspond to the times where the velocity signal of Figure 3.14 is near its maxima and minima, i.e. the acceleration changes sign.

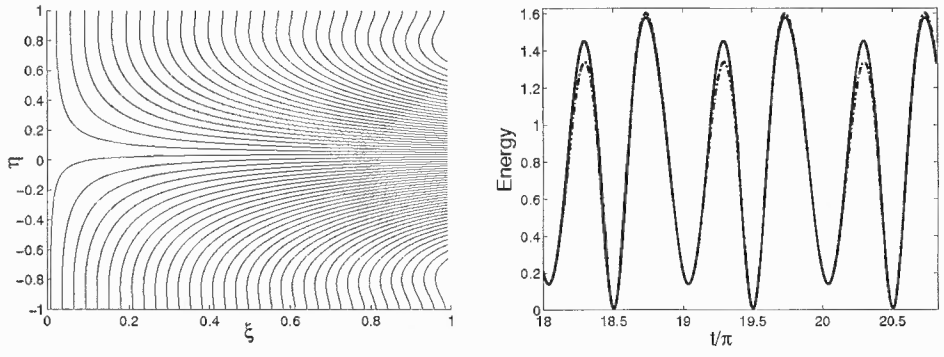

Figure 3.15 Streamlines of the Navier-Stokes flow at time $t = 20.8205\pi$ computed in the case $\Delta = 0.45$ and $R = 10$. At the right panel we show the kinetic energy of the Navier-stokes solution (solid line) and self-similar flow (dash-dot line) in the same case. The aspect ratio of the channel is $\delta = 0.01$.

Increasing the value of the Reynolds number –which corresponds to increasing the frequency of the oscillations of the walls in the present case– results in the destabilization of the self-similar Navier-Stokes flow, as can be seen in Figure 3.16. The kinetic energy curve shows oscillations with secondary frequencies additional to the driving frequency of the walls. These are the result of wave-like spatial structures which have length scales smaller than the length of the channel (see Figure 3.18 for an example). This situation is completely analogous to the case of flow driven by accelerating or decelerating walls (see Section 2.4.2, Figures 2.10 and 2.13).

Our simulations indicate that changes in the value of the oscillation amplitude Δ greatly affect the location, in terms of the Reynolds number, where the self-similar Navier-Stokes flow losses stability. In Figure 3.17 we show the time evolution of the kinetic energy and velocity signal $u(1/2,0,t)$ for the Navier-Stokes flow (solid lines) and self-similar flow (dash-dot lines) in the case $\Delta = 0.1$ and $R = 150$. As these results show, when the amplitude

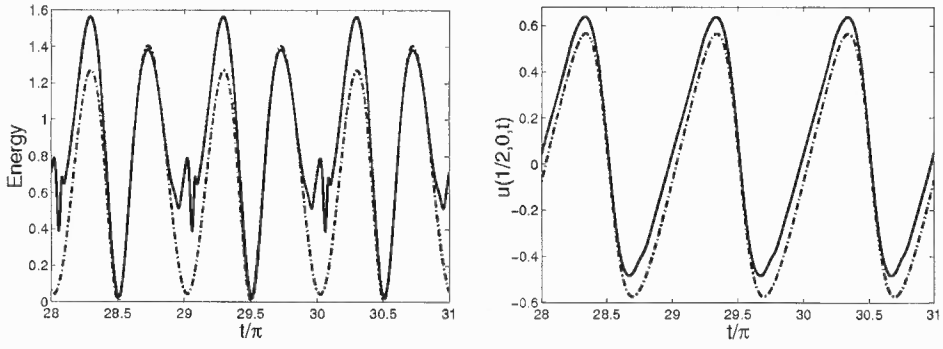

Figure 3.16 Time evolution of the kinetic energy (left panel) and velocity signal $u(1/2,0,t)$ in the case $\Delta = 0.45$ and $R = 30$. Solid line, Navier-stokes computations. Dash-dot line, self-similar solution. The aspect ratio of the channel is $\delta = 0.01$.

of the oscillations is small, the self-similar solution is recovered in a truncated channel even at moderately large values of R. This result is important for applications such as the model for oxygen transport and delivery that we study in Chapter 4, where it is assumed that a self-similar flow is a valid approximation in the regime of small amplitude oscillations and small Reynolds number.

When $\Delta = 0.25$ our results indicate that the self-similar Navier-Stokes flow is recovered for values of R as large as a hundred. However, for relatively large values of the oscillation amplitude, the self-similar Navier-Stokes flow losses stability at much smaller values of R. In Figure 3.18 we show the kinetic energy and streamlines computed in the case $\Delta = 0.65$ and $R = 4$ which indicate that although the Navier-Stokes flow is self-similar during a considerable portion of the period, it is no longer stable.

We note that for all the values of the oscillation amplitude considered, the values of the Reynolds number where we performed computations were considerably smaller that the corresponding value of the first, symmetry breaking bifurcation of the self-similar solution V.

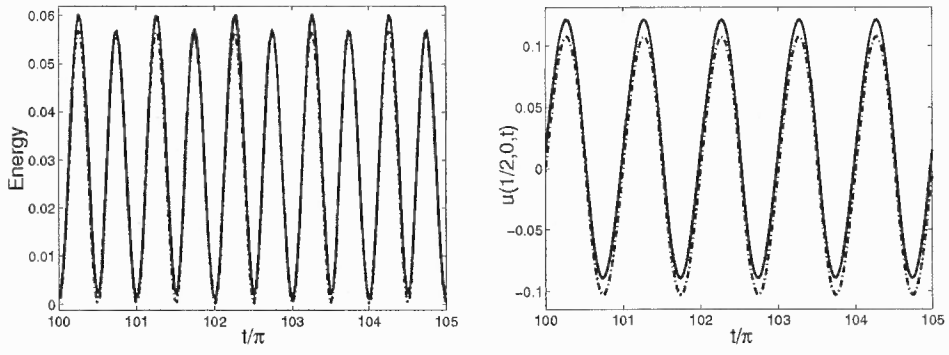

Figure 3.17 Time evolution of the kinetic energy (left panel) and velocity signal $u(1/2,0,t)$ in the case $\Delta = 0.1$ and $R = 150$. Solid line, Navier-stokes computations. Dash-dot line, self-similar solution. The aspect ratio of the channel is $\delta = 0.01$.

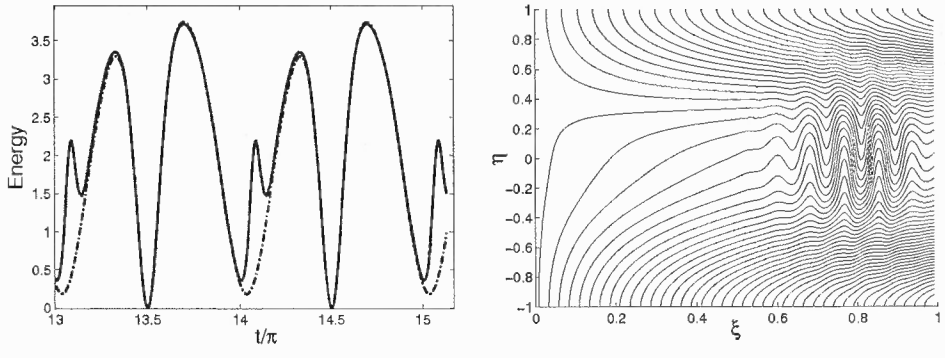

Figure 3.18 Kinetic energy of the Navier-stokes solution (solid line) and self-similar flow (dash-dot line). At the right panel we show the stream function of the Navier-Stokes flow at time $t = 15.0997\pi$. All quantities were computed in the case $\Delta = 0.65$ and $R = 4$. The aspect ratio of the channel is $\delta = 0.01$.

CHAPTER 4

SOLUTE TRANSPORT IN PULSATING CHANNELS

In this Chapter we study a two dimensional model for oxygen transport in an idealized channel, which was proposed by S. Waters (2001), Waters (2003) in an attempt to investigate how blood flow modifies oxygen delivery to the walls of laser induced revascularization vessels. These tubes are drilled in the heart muscle as part of a surgical procedure intended as a means for increasing the delivery of oxygenated blood to certain parts of the heart. As described in Waters (2001), the main purpose of that study is to gain a qualitative understanding of the basic physical mechanisms involved in the solute transport and consumption inside these channels. This is achieved by constructing an asymptotic solution to a simplified version of the model, which consists of a stagnation point type flow for an oscillating channel geometry, coupled with an advection diffusion equation for the solute (oxygen) in the channel. The medium that surrounds the channel adsorbs the solute, a process which is modeled through a diffusion equation that incorporates uptake of solute in order to account for the oxygen consumption by the muscle tissue. The solute concentration at the walls couples with the flow inside the channel through a chemical reaction boundary condition at the channel-wall interface.

Our main objective is to evaluate quantitatively the solute uptake dynamics as a function of the time periodic or aperiodic flows that derive from the self-similar Navier-Stokes solutions studied in previous chapters. As a consequence of this quantitative study, we will be able to determine a range of values of the parameters of the problem for which the asymptotic solutions of Waters (2001) provides a good approximation for the computed solutions.

In Section 4.1 we present the governing equations and the boundary conditions for this problem. In Section 4.2 we review the asymptotic solution valid in the double limit of small amplitude oscillations and large Péclet number derived in Waters (2001). In sections

4.3 and 4.4, we present our numerical results and finally in Section 4.5 we discuss several extensions and modifications of the model.

4.1 Governing Equations

We model the blood as being a homogeneous, incompressible Newtonian fluid, the oxygen in the blood as a passive solute and the muscle tissue as an homogeneous medium that absorbs oxygen at a constant rate. Since the tissue is mainly composed of water, the diffusion coefficient in the channel and in the walls are taken to be equal and the transfer of oxygen from the fluid to the walls is assumed to be controlled only by a permeability parameter. At the open end of the channel we assume that there is fluid with constant solute concentration C_0. The blood fills an oscillating channel of finite length $b(t) = b_0 b'$ and half width $a(t) = a_0 a'$ where a' and b' are given by formulas (3.28)-(3.29), i.e.

$$a' = 1 + \Delta_1 \sin \omega t,$$
$$b' = 1 + \Delta_2 \sin(\omega t + q_0).$$

We use the characteristic length and width of the channel b_0, a_0 to measure horizontal and vertical distances. Accordingly we non-dimensionalize the dependent and independent variables as follows

$$\xi = \frac{x}{b_0 b'}, \quad \eta = \frac{y}{a_0 a'}, \quad t' = \omega t, \quad u' = \frac{u}{\omega b_0}, \quad v' = \frac{v}{\omega a_0}, \quad p' = \frac{p}{\rho b_0^2 \omega^2}.$$

The non-dimensional equations of motion for the fluid inside of the channel take the form (primes dropped)

$$u_t - \xi \frac{\dot{b}}{b} u_\xi - \eta \frac{\dot{a}}{a} u_\eta + \frac{1}{b} u u_\xi + \frac{1}{a} v u_\eta = -\frac{1}{b} p_\xi + \frac{1}{R}\left(\frac{\delta^2}{b^2} u_{\xi\xi} + \frac{1}{a^2} u_{\eta\eta}\right),$$
$$v_t - \xi \frac{\dot{b}}{b} v_\xi - \eta \frac{\dot{a}}{a} v_\eta + \frac{1}{b} u v_\xi + \frac{1}{a} v v_\eta = -\frac{1}{\delta^2 a} p_\eta + \frac{1}{R}\left(\frac{\delta^2}{b^2} v_{\xi\xi} + \frac{1}{a^2} v_{\eta\eta}\right).$$

We make the assumption that the channel is slender, satisfying $\delta = a_0/b_0 \ll 1$. Under this condition we assume that the velocity field inside of the channel is well approximated by the self-similar solution (3.34)-(3.36), and given that we do not calculate the velocity field outside the channel, we assume that the velocity field is given by equations (3.34)-(3.36) everywhere in the channel, including the entrance at $\xi = 1$. This hypothesis was examined in Section 3.6 for the case of vertically oscillating flows, and it was shown to be adequate for small oscillation amplitudes and moderate values of the Reynolds number.

Let $C = C_0 C'$ be the concentration of solute in the fluid inside the channel and $\theta = C_0 \theta'$ the concentration of solute in the surrounding tissue. C satisfies the advection diffusion equation

$$C_t + \boldsymbol{u} \cdot \nabla C = D\nabla^2 C, \quad 0 \leq x \leq b, \quad -a \leq y \leq a,$$

where $\boldsymbol{u}$ is the velocity field of the fluid inside the channel and D is the diffusion coefficient of the fluid. θ satisfies the reaction diffusion equation

$$\theta_t = D\nabla^2 \theta - Q\theta, \quad 0 \leq x \leq b, \quad a \leq |y| < \infty.$$

The term $Q\theta$ represents the consumption of solute in the tissue.

The non-dimensional concentration equations are (dropping all primes)

$$C_t + \left(\frac{u}{b} - \xi\frac{\dot{b}}{b}\right) C_\xi + \left(\frac{v}{a} - \eta\frac{\dot{a}}{a}\right) C_\eta = \frac{1}{Pe}\left(\frac{\delta^2}{b^2} C_{\xi\xi} + \frac{1}{a^2} C_{\eta\eta}\right), \tag{4.1}$$

and

$$\theta_t - \xi\frac{\dot{b}}{b}\theta_\xi - \eta\frac{\dot{a}}{a}\theta_\eta = \frac{1}{Pe}\left(\frac{\delta^2}{b^2}\theta_{\xi\xi} + \frac{1}{a^2}\theta_{\eta\eta} - \lambda\theta\right), \tag{4.2}$$

where $\lambda = Qa_0^2/D$ is the ratio of consumption timescale to diffusion timescale in the surrounding medium and $Pe = \omega a_0^2/D$ is the Péclet number. In terms of the Reynolds number, $Pe = R\sigma$ where $\sigma = \nu/D$ is the Schmidt number, and ν is the kinematic viscosity of

the fluid. According to (Waters 2001), the diffusivity of oxygen in the blood is of order of magnitude $D \sim 10^{-9} m^2 s^{-1}$, the wall permeability coefficient $\beta \sim 10^{-6} m s^{-1}$, the frequency $\omega \sim 2\pi s^{-1}$, the kinematic viscosity of blood $\nu \sim 10^{-6} m^2 s^{-1}$, the rate of oxygen consumption $Q \sim 10^{-3} s^{-1}$, the width of the channel $a_0 \sim 10^{-3} m$ and the length of the channel $b_0 \sim 10^{-2} m$. These values result in the following typical values for the dimensionless parameters: $\sigma = 1000$, $Pe = 1000$, $\lambda \sim 0.2$ and $\delta = 0.05$.

In Figure 4.1 we show a definition sketch for the problem, together with the boundary conditions required for computing a numerical solution. In the remaining paragraphs of this Section we discuss each boundary condition as well as some alternatives.

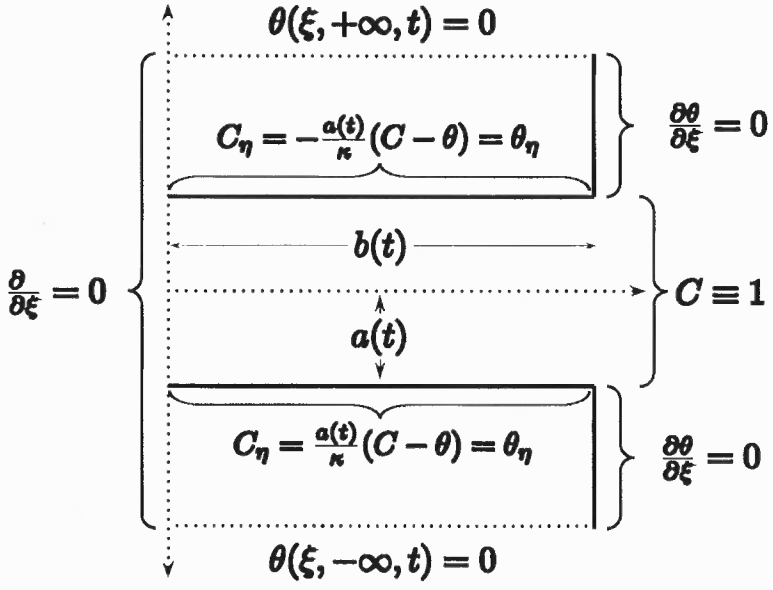

Figure 4.1 Definition sketch of the solute transport problem.

A homogeneous Neumann boundary condition at $\xi = 0$ is compatible with the stagnation point flow in the channel:

$$\theta_\xi = C_\xi = 0 \quad \text{at } \xi = 0, \tag{4.3}$$

and we assume that far away from the fluid-wall interface the wall concentration decays to zero,

$$\theta = 0 \quad \text{at } \eta = \pm\infty. \tag{4.4}$$

At the fluid-solid interface oxygen is absorbed from the fluid into the permeable walls. This effect can be thought of as an irreversible chemical reaction and can be described with the equation:

$$D\nabla C \cdot \hat{n} = -\beta(C - \theta), \tag{4.5}$$

which indicates that the rate at which this transference occurs is proportional to the difference of concentrations between the two media. The parameter β measures the permeability of the wall. If we require also the solute flux to be continuous at the interface, after non-dimensionalization , the interfacial boundary condition takes the form

$$C_\eta = \theta_\eta = -\frac{a(t)}{\kappa}(C - \theta) \quad \text{at } \eta = 1, \tag{4.6}$$

$$C_\eta = \theta_\eta = \frac{a(t)}{\kappa}(C - \theta) \quad \text{at } \eta = -1. \tag{4.7}$$

The non-dimensional parameter $\kappa = D/\beta a_0$ is the ratio of the timescales of uptake to diffusion as we will see below, and is of order one in applications. If we denote the tissue concentration at the upper interface $\theta(\xi, 1, t)$ by θ_i, according to Purnama (1995) and Boddington and Clifford (1983), the concentration of solute at the interface between a liquid and a solid which reacts with the solute present in the liquid is given by the two equations below:

$$D\nabla C \cdot \hat{n} = -\beta \frac{\partial}{\partial t}\theta_i, \tag{4.8}$$

where θ_i satisfies

$$\frac{\partial}{\partial t}\theta_i(\xi, t) = C(\xi, 1, t) - \theta(\xi, 1, t). \tag{4.9}$$

The first term on the right hand side of (4.9) represents the solute adsorbed from the fluid and the second term represents the solute leaving the tissue; the coefficients in front of the two terms are equal since in this model the channel walls represent heart muscle which is mainly composed by water, as is the fluid in the channel. For more details about these boundary conditions for flows in reacting media see Purnama (1995) and Boddington and Clifford (1983).

We will see in Section 4.2 that in the asymptotic limit of small δ the longitudinal diffusion is neglected. This results in effectively ignoring solute diffusion at the wall ends, and as a consequence a boundary condition for $\theta(1,\eta,t)$ is not necessary. On the other hand we need a boundary condition for $\theta(1,\eta,t)$ in order to do numerical computations. We impose a homogeneous Neumann condition which implies that there is no change of properties of θ at the wall ends. We find numerically that this boundary condition gives results that are in good agreement with the asymptotic solution derived in Section 4.2. As an alternative we have also used a homogeneous Dirichlet condition, for matching the outer wall concentration. Such a boundary condition introduces a layer near the wall ends at $\xi = 1$ which can be resolved by taking enough discretization points, even though the effect is artificial.

In order to set the boundary condition for the channel concentration C at the channel entrance $\xi = 1$, we need to consider the relative size of the advective terms with respect to the diffusive terms in the equation for the solute flux at the channel entrance. When the advective terms are dominant, to leading order the equation for C is hyperbolic, and can in principle be solved by the method of characteristics. As the walls of the channel move laterally apart, fluid is sucked into the channel, and assuming that mixing outside the channel occurs rapidly enough, we also assume that fluid with solute at concentration C_0 will enter the channel. As the walls contract fluid is expelled and the solute leaving the channel will depend on the concentration of the solute upstream. In other words we assume

that the solute flux at the channel end

$$\int_{-a}^{a} \left(-uC + DC_x|_{x=b(t)}\right) dy, \tag{4.10}$$

will depend only on the advective term. Therefore the dimensionless time-dependent boundary condition for C takes the form

$$C(1,\eta,t) = 1 \text{ for } t \in [-\frac{\pi}{2}, \frac{\pi}{2}] + 2\pi n, \tag{4.11}$$

$$C_\xi(1,\eta,t) = 0 \text{ for } t \in [\frac{\pi}{2}, \frac{3\pi}{2}] + 2\pi n, \tag{4.12}$$

where $n \in \mathbb{N}$ and the time origin is chosen so that the horizontal velocity term in the channel entrance is $u(1,\eta,t_0) < 0$ in (4.11) and $u(1,\eta,t_0) > 0$ in (4.12). This boundary condition is of Danckwerts type and is appropriate for slowly varying flows; see Hydon and Pedley (1993), Smith (1988) and Danckwerts (1953).

As an alternative to (4.11)-(4.12) the Dirichlet boundary condition

$$C(1,\eta,t) = 1 \text{ for } t > 0, \tag{4.13}$$

was used by Waters (2001), since the resulting problem is more tractable from an analytical point of view. This boundary condition implies that the time–average of the solute flux (4.10) depends only on the diffusive term, as follows from taking $C(1,\eta,t) \equiv 1$ and replacing u by the horizontal similarity flow $b\xi U$ of Section 3.4. It follows from equations (3.34)-(3.39) that the first term in (4.10) will depend only on the values of the vertical similarity flow V at the boundaries and the periodic function $a(t)$, thus the time average of this quantity is zero.

Numerical simulations of this problem are performed in Section 4.3 and both boundary conditions are implemented and compared. Also a comparison of the numerical and asymptotic results of Section 4.2 is presented in sections 4.3 and 4.4.

4.2 Solution Valid in the Small Amplitude Oscillations–Large Péclet Number Limit

An asymptotic solution valid in the double limit of small amplitude oscillations-large Péclet number was derived by Waters (2001). In this Section we re-derive this approximate solution because a good understanding of it is important when boundary conditions are chosen for the truncated domain used in numerical computations, and also because we are interested in comparing this asymptotic solution with our numerical solution.

When the amplitude of the oscillations of the channel is small, $\Delta_1 = \Delta_2 = \varepsilon \ll 1$, we expand the velocity field U, V in powers of ε as follows:

$$V(\eta,t) = \varepsilon[V^{[11]}(\eta)e^{it} + c.c] + \varepsilon^2[(V^{[20]}(\eta) + c.c) + (V^{[22]}(\eta)e^{2it} + c.c)] + \ldots \quad (4.14)$$

and similarly for U. The term c.c stands for complex conjugate. Because of the small amplitude we expect that the leading order velocity field will have the same frequency as the channel oscillations. The second order terms are decomposed as shown to balance the terms that appear as result of the nonlinear terms in equation (3.37). This includes the steady streaming term $V^{[20]}$.

The term $V^{[11]}$ is computed straightforwardly from equations (3.37)-(3.39):

$$V^{[11]} = \frac{1}{E}\left\{\frac{\sinh(k\eta)}{k} - \frac{\cosh(k)}{2}\eta - \frac{\sinh(k)}{2k}\eta\right\}, \quad (4.15)$$

with $k = \sqrt{R}e^{i\pi/4}$ and $E = \cosh(k) - \sinh(k)/k$. The next two terms were calculated with the help of Maple:

$$\begin{aligned} V^{[20]} = R\Bigg\{ & i\frac{\sinh(k\eta)}{Ek} - \frac{1}{2E\bar{E}}\left[\frac{\bar{k}^2\sinh(\bar{k}\eta + k\eta)}{k(\bar{k}+k)^4} + \frac{\bar{k}^2\sinh(k\eta - \bar{k}\eta)}{k(k-\bar{k})^4}\right. \\ & - \left(\frac{\sinh(k)}{k} + \cosh(k)\right)\left(\frac{\eta\cosh(\bar{k}\eta)}{\bar{k}^2} - 5\frac{\sinh(\bar{k}\eta)}{\bar{k}^3}\right) - \frac{\bar{k}\sinh(\bar{k}\eta + k\eta)}{(\bar{k}+k)^4} + \\ & \left.\frac{\bar{k}\sinh(k\eta - \bar{k}\eta)}{(k-\bar{k})^4}\right] - \frac{1}{2Ek^3}\Big(k\eta\cosh(k\eta) - 2\sinh(k\eta)\Big)\Bigg\}, \end{aligned} \quad (4.16)$$

and

$$V^{[22]} = \frac{R}{4k^4E^2}\Big(k(1-x)\sinh(k+k\eta)+(1-k^2\eta)\cosh(k+k\eta) \\ +k(1+\eta)\sinh(k\eta-k)-(1+k^2\eta)\cosh(k\eta-k) \\ +2k^2E\cosh(k\eta)\eta+4kE\left(1+i\frac{k^2}{R}\right)\sinh(k\eta)\Big). \quad (4.17)$$

Bars denote complex conjugates. We look for solutions of the concentration equations (4.1)-(4.2) in the form:

$$C(\eta,\xi,t) = \mathscr{C}(\eta,\xi)+\varepsilon[C^{[11]}(\eta,\xi)e^{it}+c.c]+O(\varepsilon^2), \quad (4.18)$$

$$\theta(\eta,\xi,t) = \Theta(\eta,\xi)+\varepsilon[\theta^{[11]}(\eta,\xi)e^{it}+c.c]+O(\varepsilon^2). \quad (4.19)$$

If we ignore the $O(\delta^2)$ terms and expand equations (4.1)-(4.2) in powers of ε we find that at leading order

$$C^{[11]} = i(-\frac{1}{2}\eta+V^{[11]})\frac{\partial\mathscr{C}}{\partial\eta}+i\xi(-\frac{1}{2}+V_\eta^{[11]})\frac{\partial\mathscr{C}}{\partial\xi}. \quad (4.20)$$

To obtain the governing equation for $\mathscr{C}$ we substitute the expression for $C^{[11]}$ above and computing the time–average of the equation for $O(\varepsilon^2)$ terms over a period

$$\xi\mathscr{U}\frac{\partial\mathscr{C}}{\partial\xi}+\mathscr{V}\frac{\partial\mathscr{C}}{\partial\eta} = \frac{1}{\tilde{p}}\frac{\partial^2\mathscr{C}}{\partial\eta^2}, \quad (4.21)$$

where $\mathscr{U} = V_\eta^{[20]} - iV_{\eta\eta}^{[11]*}(-\eta/2+V^{[11]})+c.c.$ and $\mathscr{V} = V^{[20]}+i(1/2-V_\eta^{[11]*})(-\eta/2+V^{[11]})+c.c.$. The asterisk denotes complex conjugate. The steady streaming Péclet number $\tilde{p} = \varepsilon^2 Pe$ is defined based on the form of the expansion for the velocity field and allows us to obtain the meaningful balance shown in equation (4.21); the transverse diffusive term would dominate otherwise.

In a similar way the governing equation for Θ can be derived from the equation for

$O(\varepsilon^2)$ terms in the expansion of θ, by replacing the identity for $\theta^{[11]}$ which results from the $O(\varepsilon)$ equation and by taking a time-average over a period:

$$\frac{\partial^2 \Theta}{\partial \eta^2} - \lambda \Theta = 0. \tag{4.22}$$

The solution for $\eta > 1$ is given

$$\Theta = A(\xi) \exp(-\lambda^{1/2} \eta), \tag{4.23}$$

The unknown A depends on $\mathscr{C}$ and is found from the interfacial boundary condition. For $\eta < -1$ the solution has the sign inside the exponential reversed.

Equation (4.21) can further simplified by assuming that $\varepsilon \ll \tilde{p} \ll 1$. If $\tilde{p}$ is small, the transverse diffusive term in equation (4.21) is dominant and it tends to equilibrate the concentration of solute across the channel, allowing us to seek an approximation in powers of $\tilde{p}$ as shown below. The assumption $\varepsilon \ll \tilde{p} \ll 1$ is compatible with the previous expansions, and it only restricts the value of the Péclet number to the range $\varepsilon^{-1} \ll Pe \ll \varepsilon^{-2}$.

We expand $\mathscr{C}$ as follows

$$\mathscr{C} = \widehat{\mathscr{C}}(\xi) + \tilde{p}\mathscr{C}^{(1)}(\xi, \eta), \tag{4.24}$$

where by definition $\widehat{f}$ means $\int_0^1 f d\eta$, i.e. we are decomposing $\mathscr{C}$ in its η-average plus small fluctuations (by definition $\mathscr{C}^{(1)}$ contains all powers of $\tilde{p}$). Note that we only consider positive values of η in this expansion since for small oscillation amplitudes and small Reynolds numbers the flow is symmetric about $\eta = 0$. By expanding all terms in equation (4.21) in powers of $\tilde{p}$ we get

$$\xi \mathscr{U} \left(\frac{\partial \widehat{\mathscr{C}}}{\partial \xi} + \tilde{p} \frac{\partial \mathscr{C}^{(1)}}{\partial \xi} \right) + \tilde{p} \mathscr{V} \frac{\partial \mathscr{C}^{(1)}}{\partial \eta} = \frac{\partial^2 \mathscr{C}^{(1)}}{\partial \eta^2}, \tag{4.25}$$

which at leading order is

$$\mathscr{C}^{(1)} = \xi \frac{\partial \widehat{\mathscr{C}}}{\partial \xi} \int_0^\eta \mathscr{F}(s)ds \text{ where } \mathscr{F} = \int_0^\eta \mathscr{U}(s)ds. \tag{4.26}$$

By integrating equation (4.25) with respect to η between 0 and 1 we get

$$\tilde{p}\xi \widehat{\mathscr{U}\mathscr{C}_\xi^{(1)}} + \tilde{p}\widehat{\mathscr{V}\mathscr{C}_\eta^{(1)}} = \frac{\partial \mathscr{C}^{(1)}}{\partial \eta}|_{\eta=1}. \tag{4.27}$$

With the help of Maple one can show that the η-average of $\mathscr{U}$ is zero, which implies that the first term in (4.25) is gone after the averaging. If we expand all the terms in the interfacial boundary condition (4.6)-(4.7) in powers of $\tilde{p}$, it follows from equation (4.23) that at leading order

$$\frac{\partial \mathscr{C}^{(1)}}{\partial \eta}|_{\eta=1} = -\frac{\Lambda}{\tilde{p}}\widehat{\mathscr{C}} \text{ where } \Lambda = \frac{\lambda^{1/2}}{1+\kappa\lambda^{1/2}}, \tag{4.28}$$

is assumed to be $O(\tilde{p})$. Thus the governing equation for $\widehat{\mathscr{C}}$ is

$$\xi^2 \frac{d^2\widehat{\mathscr{C}}}{d\xi^2} + 2\xi \frac{d\widehat{\mathscr{C}}}{d\xi} - \gamma\widehat{\mathscr{C}} = 0, \text{ where } \gamma = \frac{\Lambda}{\tilde{p}^2} \frac{1}{\int_0^1 \mathscr{F}^2 d\eta}. \tag{4.29}$$

If $\gamma \ll 1$, the leading order solution for equation (4.29) which satisfies the boundary condition (4.13) is $\widehat{\mathscr{C}} = 1$, which means that in the asymptotically small solute uptake regime the solution for an impermeable channel is recovered. As is readily seen from the definition of γ

$$\gamma = \frac{1}{\tilde{p}^2} \frac{\lambda^{1/2}}{1+\kappa\lambda^{1/2}} \frac{1}{\int_0^1 \mathscr{F}^2 d\eta},$$

the limit $\gamma \ll 1$ corresponds to either $\lambda \ll 1$, $\kappa = O(1)$; or $\kappa \gg 1$, $\lambda = O(1)$, which are respectively, small solute consumption in the channel walls, and small wall permeability. In Figure 4.2 we show the ξ-average of the numerical solution of the concentration equations (4.1)-(4.2) subject to the boundary conditions described in Section 4.1, for several values

of the wall permeability parameter κ. As κ gets larger the numerical solution approaches the solution in the asymptotically small solute uptake regime. Due to the small values of $\tilde{p}$ and the average of $\mathscr{F}^2$, κ has to be very large in order to compensate for these two factors.

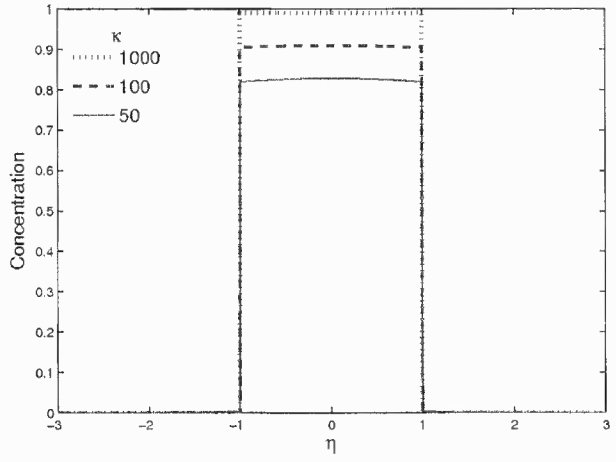

Figure 4.2 ξ-average of the channel and wall solute concentrations for several values of κ. ($\varepsilon = 0.01, R = 1, \sigma = 1000, \lambda = 20, \delta = 0.01$).

In the large wall permeability regime, which corresponds to $\gamma \gg 1$, $\widehat{\mathscr{C}} = 0$ except at small distances from the channel entrance. We can analyze this region by introducing the stretched variable $z = \sqrt{\gamma}(1-\xi)$ to find that the solution satisfying $\widehat{\mathscr{C}}(0) = 1, \widehat{\mathscr{C}}(\infty) = 0$ is $\widehat{\mathscr{C}}(z) = \exp(-z)$. In terms of the original variables this solution is

$$\widehat{\mathscr{C}} = \exp\left\{ -\frac{1}{\tilde{p}} \frac{1}{\int_0^1 \mathscr{F}^2 d\eta} \sqrt{\frac{\lambda^{1/2}}{1+\kappa\lambda^{1/2}}} (1-\xi) \right\}. \tag{4.30}$$

From equation (4.6), it follows that the leading order solution for the concentration in the surrounding tissue region is

$$\Theta = \frac{1}{1+\kappa\lambda^{1/2}} \widehat{\mathscr{C}} \exp\{\lambda^{1/2}(1-\eta)\}. \tag{4.31}$$

The asymptotic solution (4.30) is not valid at distances $O(\tilde{p})$ from the channel entrance. In this region the horizontal advective term in equation (4.21) is comparable to the

otherwise dominant diffusive term. This implies that γ must satisfy $\tilde{p} \ll \gamma^{-1/2} \ll 1$ as seen from the definition of the stretched variable z.

In the present regime, the advective term in the solute flux at the channel entrance dominates the diffusive term since the ratio of the characteristic steady advection to longitudinal diffusion in this region is $O(\tilde{p}/\delta^2)$. Thus, the boundary condition of choice for the channel entrance should be (4.11)-(4.12). Comparisons between the results obtained by using the 'advective' boundary condition and the 'diffusive' one (equation (4.13)) are shown in the next Section.

4.3 Numerical Solution and Results

We discretize equations (4.1)-(4.2) with a Peaceman-Rachford ADI scheme. Spatial discretizations are done in a uniform grid and all spatial derivatives are approximated with centered differences with the exception of the advective terms which are approximated with upwind first order finite differences. In order to compare the numerical results with the asymptotic solution derived in Section 4.2 we use the boundary condition (4.13) at the channel entrance, but we also present computations were the boundary condition (4.11)-(4.12) was employed. We indicate which boundary condition was used in each case. It is expected from the asymptotic solution (4.31) that the concentration in the surrounding media will decay very fast away from the fluid-tissue interface at $\eta = \pm 1$. Accordingly we truncate the domain for calculations in the vertical direction from $\eta = -3$ to $\eta = +3$ and we impose a homogeneous Dirichlet condition at these boundaries. We find that these conditions produce results that are consistent with the asymptotic computations of the previous Section. A detailed description of the numerical scheme is given in Appendix B.

As explained in Section 4.1, the typical values for the non-dimensional parameters in this problem are $\sigma = 1000$, $Pe = 1000$, $\kappa \sim 0.5$ and $\lambda \sim 0.2$. In all the numerical calculations we set $\delta = 0.01$, which is appropriate given that a value $\delta = 0.05$ results from the typical radius and length of a revascularization channel. The amplitude is fixed at the

value $\Delta = 0.01$.

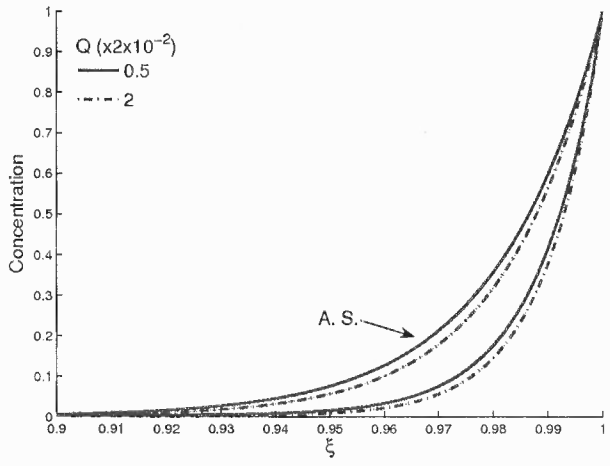

Figure 4.3 Solute concentration in the channel, $\widehat{\mathscr{C}}(\xi)$ for several values of the solute consumption Q. ($\sigma = 1000$, $\kappa = 0.5$, $R = 4$). The curves labeled with $A.S$ were obtained with the asymptotic solution (4.30).

As follows from formula (4.30), $\widehat{\mathscr{C}}$ depends on the consumption rate Q through λ, and for any value of ξ, $\widehat{\mathscr{C}}$ decreases as Q increases. We were able to reproduce this dependency as can be seen in the plots of $\widehat{\mathscr{C}}$ versus ξ of Figure 4.3. The solution in the large wall permeability regime of these computations is zero everywhere except at small distances from the channel entrance. Considering that the study presented in Waters (2001) is essentially a qualitative one and that several parameters and boundary conditions should be adjusted to provide a better fit between numerical and asymptotic solutions, we consider the agreement between the numerical and asymptotic solutions shown in Figure 4.3 satisfactory for our purposes.

In Figure 4.4 we show the solute concentration of the tissue at the wall-fluid interface $\Theta|_{\eta=1}$, as a function of ξ for several values of the wall permeability β. Θ depends on β through the dimensionless parameter κ. As can be seen from equation (4.31), away from the channel entrance Θ decreases as the wall permeability at the interface increases. Θ is proportional to $\widehat{\mathscr{C}}$, which decreases with increasing β, as the solute passes more easily through the interface to be consumed in the surrounding tissue. The situation is reversed near the channel entrance where the availability of solute from outside the channel is not

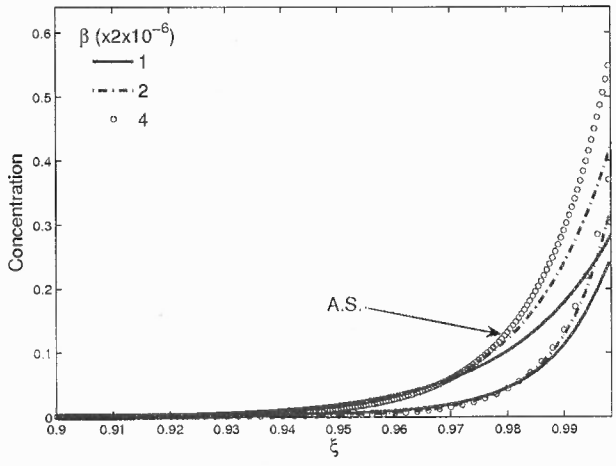

Figure 4.4 Solute concentration in the medium at the interface, $\Theta|_{\eta=1}(\xi)$ for several values of the wall permeability β ($\sigma = 1000$, $\lambda = 20$, $R = 4$). The curves labeled with *A.S* were obtained with the asymptotic solution (4.30).

a limitation. Away from the interface the solute concentration decays exponentially at an approximate rate of $\lambda^{1/2}$ as follows from formula (4.31).

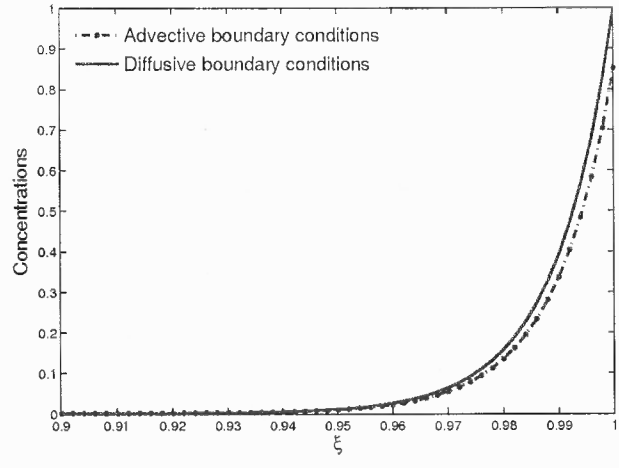

Figure 4.5 Solute concentration in the channel, $\widehat{C}$, versus ξ. Dash-dotted line obtained with scheme implementing the boundary condition (4.11)-(4.12). ($\sigma = 1000$, $\kappa = 0.5$, $\lambda = 20$, $R = 4$)

We computed concentrations for several values of the consumption rate Q using boundary conditions (4.11)-(4.12) instead of boundary condition (4.13) at the channel entrance. For the sake of clarity we only present two curves for $\widehat{\mathscr{C}}(\xi)$ in Figure 4.5 each one of them obtained with a boundary condition indicated by the corresponding label: either

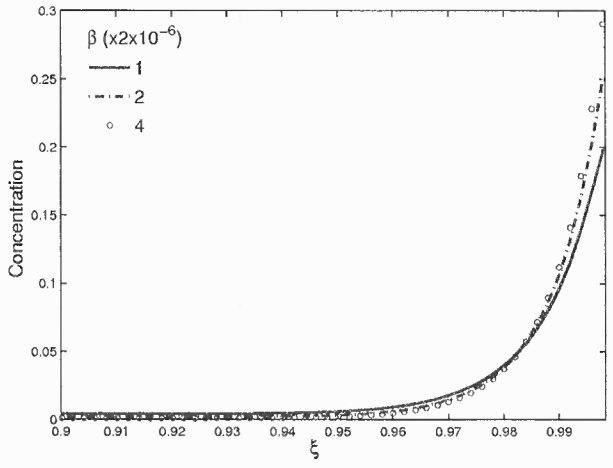

Figure 4.6 Solute concentration in the medium at the interface, $\Theta|_{\eta=1}$, versus ξ for several values of the wall permeability β. This results were produced with the advective boundary condition version of the scheme ($\sigma = 1000$, $\lambda = 20$, $R = 4$).

the 'advective' boundary condition given by equations (4.11)-(4.12) or the 'diffusive' one given by equation (4.13). As shown in Figure 4.5, $\widehat{\mathscr{C}}(\xi = 1)$ is no longer 1 because the 'advective' condition does not require the concentration to be identically 1 at the channel entrance. The qualitative agreement between the time averaged concentrations indicates that the choice of equation (4.13) as boundary condition produces reasonable results for the given values of the governing parameters. In Figure 4.6 we show the wall concentration at the interface obtained when we repeated the calculations using boundary condition (4.11)-(4.12). The behavior of $\Theta(\xi, \eta = 1)$ as a function of β is qualitatively the same as observed in our previous computations for Θ using the 'diffusive' boundary condition (4.13).

4.4 Computations Beyond the Range of Asymptotic Validity: Effects of Oscillation Amplitude and Péclet Number

The asymptotic solution (4.30)-(4.31) is valid in the double limit of small oscillation amplitude and large Péclet number. A natural question that arises in the present study is how the delivery of solute is influenced by the value of the oscillation amplitude. We address

this question by studying the evolution of the Nusselt number that we define as follows:

$$\langle N \rangle = \frac{1}{2\pi} \int_{t_0}^{t_0+2\pi} \int_0^{b(t)} DC_y|_{y=a(t)} dx dt. \tag{4.32}$$

This quantity is a measure of the amount of solute that leaves the channel through the interface at $y = a(t)$. $\langle N \rangle$ is a function of λ, κ, σ, R and Δ, the amplitude of vertical and horizontal oscillations which here is taken to be equal. The Nusselt number for the interface at $y = -a(t)$ is defined in a similar way and we compare both quantities when the Reynolds number is larger than approximately 39, and the flow (3.37) has lost symmetry about $\eta = 0$. Since the dependency of the solute concentration on λ and κ is well explained by the asymptotic formulas obtained in the previous Section, we keep these two parameters and σ fixed and we compute $\langle N \rangle$ as a function of the Reynolds number and Δ. For all the calculations presented in this Section we set $\lambda = 20$, $\kappa = 0.5$, $\sigma = 1$, so that $Pe = R$.

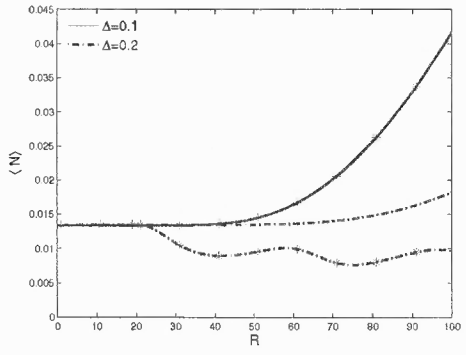

Figure 4.7 $\langle N \rangle$ as a function of the Reynolds number for small oscillation amplitudes, $\Delta \leq 0.2$.

In Figure 4.7 we present several curves of $\langle N \rangle$ as a function of R for amplitude values $\Delta \leq 0.2$ obtained by integrating the equations for the concentrations numerically. The starred curves were obtained by using the explicit formulas for the asymptotic velocity presented in Section 4.2, and the un-starred curves were obtained by solving equations (3.37)-(3.39) numerically. As we can see in the Figure, when $\Delta = 0.1$ the asymptotic and numerical computations are indistinguishable for a sizable range of Reynolds numbers (this is true also for smaller values of Δ). However, for the relatively small value $\Delta = 0.2$ the

region where the asymptotic formulas for the velocity produce reasonable results is much smaller. This behavior is maintained and the region of agreement shrinks with increasing Δ.

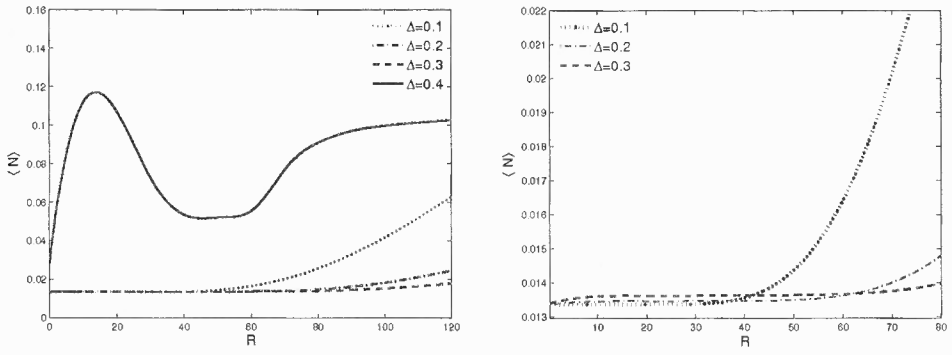

Figure 4.8 $\langle N \rangle$ as a function of the Reynolds number for several values of Δ. The second plot is an enlargement of the first plot.

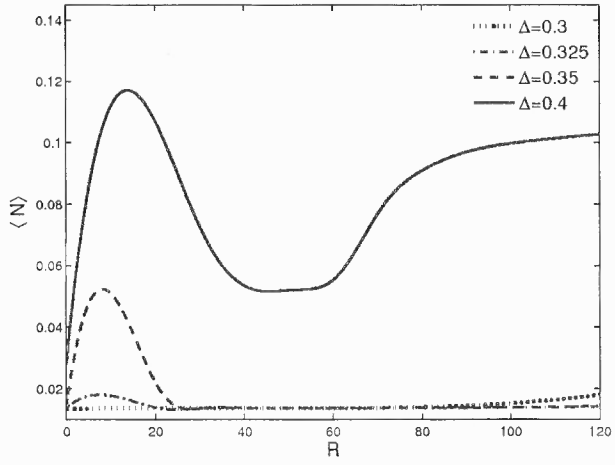

Figure 4.9 $\langle N \rangle$ as a function of the Reynolds number when $0.3 \leq \Delta \leq 0.4$.

For $\Delta = 0.4$ the effects of the nonlinear velocity field are evident as can be seen in the results of Figure 4.8. At this value of the oscillation amplitude the Nusselt number is no longer a monotonic function of R. The curve has local maxima and local minima, and the first local maximum is attained at relatively small values of R. In Figure 4.9 we plotted additional $\langle N \rangle$-R curves in the range of $0.3 \leq \Delta \leq 0.4$ to show the transition between monotonic and non-monotonic behavior better. As seen in Chapter 3, at sufficiently large values of the Reynolds number the flow V loses symmetry around $\eta = 0$ due to a symmetry

breaking bifurcation. In Figure 4.10 we show the Nusselt number calculated at the lower and upper interfaces in the case $\Delta = 0.4$. In this case the symmetry breaking bifurcation takes place at a value $R \sim 39$ and for values of R above 60 the difference between the amount of solute leaving through the upper and lower walls is considerable. Considering the values of the oscillation amplitude and Reynolds numbers for the results presented in Figures 4.8 through 4.10, together with the results presented in Section 3.6 for a vertically oscillating channel, we conclude that for values of Δ greater than 0.2, numerical simulations should be carried out without assuming that the flow at the interior of the channel is of self-similar form.

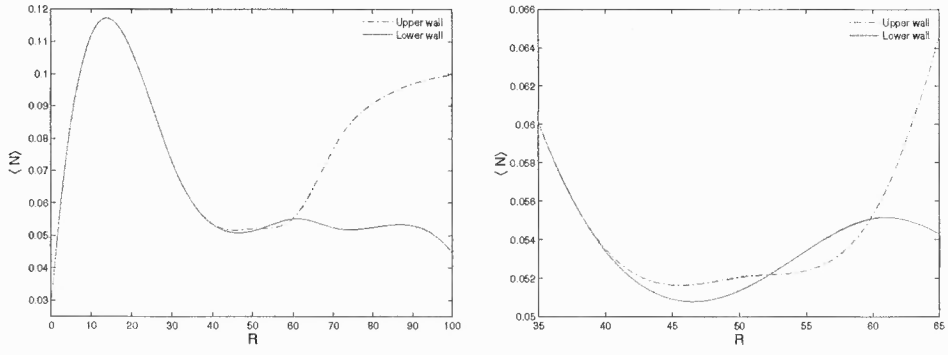

Figure 4.10 $\langle N \rangle$ calculated at the upper and lower wall-fluid interfaces in the case ($\Delta = 0.4$). The second plot is an enlargement of the first plot.

4.5 Conclusions and Future Work

The numerical results of Section 3.6, show that for small values of the oscillation amplitude (in the case of vertically oscillating walls this means $\Delta \lesssim 0.2$) a self-similar flow is a very robust model for the flow driven by the movements of the walls. On the other hand, in applications where results for $O(1)$ values of the Reynolds number and larger values of the oscillation amplitude are of interest, it is necessary to solve the Navier-Stokes equations directly without assuming that a self-similar solution will produce reasonable results. Accordingly, it would be necessary to recalculate the results shown in Figures 4.8 through 4.10, by coupling equations (3.30)-(3.32) to the concentration equations (4.1)-(4.2) directly,

without assuming a special form for the velocity field and the pressure.

The asymptotic solution of Section 4.2 gives us a basic understanding of how the concentration of solute depends on the governing parameters of the model. Equipped with this knowledge we can now pursue studying more sophisticated models numerically. An obvious extension would be coupling the solution to the equations of motion of Section 3.6 (in the case of non-zero lateral oscillation amplitude) with the concentration equation (4.1) directly without assuming that the flow is of self similar form. As seen in Section 3.6, for relatively large values of the oscillation amplitude, the difference between the Navier-Stokes flow and self-similar solution can be significant even at order one values of the Reynolds number. Also in cases of smaller oscillation amplitudes, the discrepancy between the imposed self-similar solution at the channel entrance and the flow at the interior of the channel might produce changes in the solute concentration near the channel entrance that have to be investigated.

For simplicity, we assumed in equation (4.2) that the solute consumption term was linear. This assumption is reasonable when the wall concentration is small. It would be more realistic to take into account the effect of cell saturation by modifying the solute consumption term to

$$-Q\frac{\theta^2}{\theta^2+\alpha}, \tag{4.33}$$

where α is a constant. When θ is large this term is nearly constant equal to $-Q$, and corresponds to consumption in a saturated state (see Murray (2003*a*), page 7 and Murray (2003*b*), page 263).

A related problem of self-similar oscillatory flow in a cylindrical tube was studied by Blyth, Hall and Papageorgiou (Blyth et al. 2003). In that paper, it was found that with the exception of the behavior at small Reynolds numbers the dynamics of the axisymmetric flow differs considerably from the dynamics of the two-dimensional case. As in the channel flow, the dynamics depend on R and Δ, and for any value of the oscillation amplitude a Hopf bifurcation takes place as R increases. They also found that, in a sharp contrast with

the channel case, for values $\Delta < 0.2$ and values $\Delta > 0.45$ chaotic behavior is not observed. These differences for self-similar flows between channel geometries and axisymmetric geometries, together with the asymptotic study of O'dea and Waters (2006) of solute transport and uptake in twisting tubes, motivate future extensions of the work of Sections 3.6 and 4.3 to the axisymmetric case.

APPENDIX A

NAVIER–STOKES SOLVER

The time discretization uses a forward Euler scheme treating the pressure terms implicitly while the viscous and convective terms are explicit (see (A.4)-(A.5) below). Stability is maintained by adapting the time-step so that a CFL condition is satisfied (see Griebel et al. (1998), Tome and McKee (1994)). The incompressibility equation is used to derive a Poisson equation for the pressure at time t_{n+1} which has the form

$$\Delta p^{n+1} = \frac{R}{\Delta t}\left\{F_x{}^n + G_y{}^n\right\}, \tag{A.1}$$

where

$$F^n = u^n + \Delta t\left\{\frac{1}{R}(u_{xx}+u_{yy})^n - (u^2)_x{}^n - (uv)_y{}^n\right\}, \tag{A.2}$$

$$G^n = v^n + \Delta t\left\{\frac{1}{R}(v_{xx}+v_{yy})^n - (v^2)_y{}^n - (uv)_x{}^n\right\}. \tag{A.3}$$

Once p^{n+1} has been computed the velocity field is updated according to the equations below

$$u^{n+1} = F^n - \frac{\Delta t}{R}\left(p_x{}^{n+1}\right), \tag{A.4}$$

$$v^{n+1} = G^n - \frac{\Delta t}{R}\left(p_y{}^{n+1}\right). \tag{A.5}$$

Spatial derivatives are discretized on a uniform staggered grid in the following way: the pressure is evaluated in the middle of the discretization cells, u at the midpoints of the vertical edges of the cells (the x-momentum equation (A.4) is discretized at the same points) and v is evaluated at the midpoints of the horizontal cell edges (the y-momentum equation (A.5) is also discretized at these points), see Figure A.1.

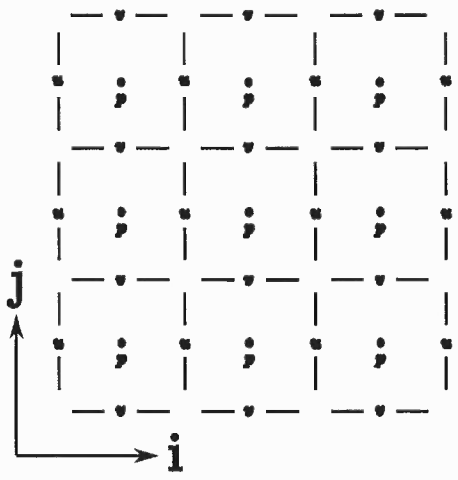

Figure A.1 The staggered grid for the discretization of the Navier-Stokes equations.

All the spatial derivatives are approximated with centered differences with the exception of the nonlinear advective terms in equations (A.4) and (A.5) which are approximated by using an average of centered differences and upwind differences to obtain a higher order, stable discretization. Fictitious points are introduced outside the computational domain in order to maintain second order accuracy for the boundary conditions. A numerical boundary condition is required for solving the Poisson equation (A.1) and is found as follows: let $\hat{n} = (n_1, n_2)$ be the unit normal vector to the boundary of the domain Ω at (x,y). Then from equations (A.4) and (A.5)

$$n_1 u^{n+1} = -n_1 \frac{\Delta t}{R} \left(p_x{}^{n+1}\right) + n_1 F^n,$$
$$n_2 v^{n+1} = -n_2 \frac{\Delta t}{R} \left(p_y{}^{n+1}\right) + n_2 G^n,$$

thus

$$\frac{\Delta t}{R}(p_x{}^{n+1}, p_y{}^{n+1}) \cdot (n_1, n_2) = n_1(F^n - u^{n+1}) + n_2(G^n - v^{n+1}),$$
$$\frac{\partial p^{n+1}}{\partial \hat{n}} = \frac{n_1 R}{\Delta t}(F^n - u^{n+1}) + \frac{n_2 R}{\Delta t}(G^n - v^{n+1}).$$

Noting that homogeneous Neumann boundary conditions are compatible with the equations

of motion as can be seen from the equations above, we conclude that the discretization of equation (A.1) using homogeneous Neumann boundary conditions, produces a singular linear system with a matrix that has a block TST (Toeplitz, symmetric and tridiagonal) structure. As explained by Griebel et al. (1998) this singular system can be replaced by an approximate non-singular system which results from replacing the homogeneous Neumann conditions with the approximate Dirichlet conditions

$$p_{0j}^{n+1} = p_{1j}^{n}, \quad p_{i_M j}^{n+1} = p_{i_M - 1 j}^{n} \quad j = 1, \ldots, j_M, \tag{A.6}$$

$$p_{i0}^{n+1} = p_{i1}^{n}, \quad p_{i j_M}^{n+1} = p_{i j_M - 1}^{n} \quad i = 1, \ldots, i_M. \tag{A.7}$$

This numerical scheme can be validated by comparing the numerical solution with the *Beltrami* flow:

$$u = -\cos(x)\sin(y)\exp(-2t/R), \tag{A.8}$$

$$v = \sin(x)\cos(y)\exp(-2t/R), \tag{A.9}$$

$$p = R\left(\frac{\sin(x)^2 + \sin(y)^2}{2} - 1\right)\exp(-4t/R), \tag{A.10}$$

which is an exact solution of the Navier-Stokes equations in a $[0 \ \pi] \times [0 \ \pi]$ square (see Section 4.6 of the Book by Drazin and Riley (2006) for a description of Beltrami flows). The pressure term satisfies homogeneous Neumann conditions at the boundary of the square $[0 \ \pi] \times [0 \ \pi]$, and our extensive numerical experiments show that the errors introduced by the change from Neumann to Dirichlet conditions are small enough that do not compromise the second order spatial accuracy of the scheme. In Figure A.2 below, we plotted the error defined as the Frobenius norm of the difference between the exact velocity field shown in equations (A.8)-(A.10) and the numerical solution computed by imposing initial and boundary conditions according to the same Beltrami flow. Since the pressure (A.10) is unique up to a constant, it is not possible to compare the exact and numerical pressures

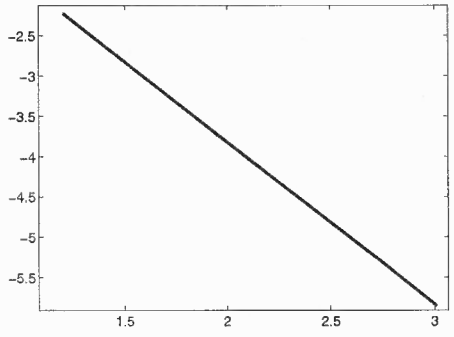

Figure A.2 Log-log plot of error for increasing grid sizes. The slope of the curve is -2.0005.

directly. Several direct comparisons for computed pressure gradients have been shown in Chapter 2, see for example Figures 2.11 and 2.7.

Typical grid sizes for all the computations reported in this document range from 256×256 to 1024×1024 uniform meshes. Several accuracy tests were performed to confirm that there was little change in the reported results when the resolution is increased. Most runs are therefore performed with a 256×256 grid. The stability condition described by Griebel et al. (1998) and Tome and McKee (1994) is satisfied by computing the velocity maximum at each iteration and defining the time-step accordingly:

$$|u_{max}|\Delta t < \Delta x, \quad |v_{max}|\Delta t < \Delta y, \quad \Delta t < \frac{R}{2}\left(\frac{1}{\Delta x^2} + \frac{1}{\Delta y^2}\right)^{-1},$$

where the first two inequalities are the *CFL* condition for this scheme. The resulting time-step can be uniformly adjusted by multiplying it with a parameter which is less than one. Typical values of this parameter are 0.5, 0.1 and 0.01, the latter used only with the most rapidly oscillating flows.

Equation (A.1) is solved efficiently with a Fast Fourier Transform based fast Poisson solver (Hockney's method). For simplicity, we describe our Poisson solver considering a very simple case:

$$\frac{p_{i+1j} - 2p_{ij} + p_{i-1j}}{\Delta x^2} + \frac{p_{ij+1} - 2p_{ij} + p_{ij-1}}{\Delta y^2} = RHS_{ij},$$

with homogeneous Dirichlet conditions. We can organize the unknowns by columns:

$$P = \begin{bmatrix} p_{11} \\ p_{12} \\ \vdots \\ p_{1 j_M} \\ p_{21} \\ \vdots \\ p_{i_M j_M} \end{bmatrix} \equiv \begin{bmatrix} P_1 \\ P_2 \\ \vdots \\ P_{i_M} \end{bmatrix}$$

and similarly with the right hand side of the equation. The resulting linear system is $AP = R$, where A has the following block form

$$A = \begin{bmatrix} B & I & & & \\ I & B & I & & \\ & \ddots & \ddots & \ddots & \\ & & I & B & I \\ & & & I & B \end{bmatrix}, \text{ and the } j_M \times j_M \text{ block } B = \begin{bmatrix} -4 & 1 & & & \\ 1 & -4 & 1 & & \\ & \ddots & \ddots & \ddots & \\ & & 1 & -4 & 1 \\ & & & 1 & -4 \end{bmatrix}.$$

The matrix B is *Toeplitz*, symmetric and tri-diagonal, and in consequence its eigenvalues and eigenvectors are known. The Lemma 10.5, from Iserles (2008) page 198, states: let T be a $d \times d$ TST matrix

$$T = \begin{bmatrix} \alpha & \beta & & & \\ \beta & \alpha & \beta & & \\ & \ddots & \ddots & \ddots & \\ & & \beta & \alpha & \beta \\ & & & \beta & \alpha \end{bmatrix},$$

then the eigenvalues of T are

$$\lambda_j = \alpha + 2\beta \cos\left(\frac{\pi j}{d+1}\right), \quad j = 1, \ldots, d,$$

with corresponding orthogonal eigenvectors $\boldsymbol{q}_j$, where

$$q_{j,l} = \sqrt{\frac{2}{d+1}} \sin\left(\frac{\pi jl}{d+1}\right), \quad j,l = 1, \ldots, d.$$

As corollaries, the matrix of eigenvectors $Q = [\boldsymbol{q}_1 \ \ldots \ \boldsymbol{q}_d]$ is orthogonal and symmetric. Also the set of $d \times d$ TST matrices is commutative with respect to multiplication (see Iserles (2008) for the proofs). These properties of TST matrices allow us to simultaneously diagonalize the block form of the system $AP = R$, resulting in the block diagonal system

$$\begin{bmatrix} \Lambda & I & & & \\ I & \Lambda & I & & \\ & \ddots & \ddots & \ddots & \\ & & I & \Lambda & I \\ & & & I & \Lambda \end{bmatrix} \begin{bmatrix} Y_1 \\ Y_2 \\ \vdots \\ Y_{i_M-1} \\ Y_{i_M} \end{bmatrix} = \begin{bmatrix} C_1 \\ C_2 \\ \vdots \\ C_{i_M-1} \\ C_{i_M} \end{bmatrix}$$

where Λ is the diagonal matrix of eigenvalues of B, $C_i = QR_i$ and $P_i = QY_i$, $i = 1, \ldots, i_M$. These matrix products can be computed very efficiently by using the Fast Fourier Transform. The components of the eigenvector $\boldsymbol{q}_j$ can be written in terms of complex exponentials:

$$q_{j,l} = \sqrt{\frac{2}{j_M+1}} \operatorname{Im}\left(\exp\left(i\frac{\pi jl}{j_M+1}\right)\right), \quad j,l = 1, \ldots, j_M,$$

and as a consequence the product of any vector $\boldsymbol{z}$ with the matrix of eigenvectors Q can be computed as the inverse Fourier Transform of a vector $\hat{\boldsymbol{z}}$ of dimension $2j_M + 1$ formed by

padding $\boldsymbol{z}$ with zeros:

$$Q\boldsymbol{z} = \mathscr{F}^{-1}(\hat{\boldsymbol{z}}), \quad \hat{\boldsymbol{z}} = [0, z_1, \ldots, z_{j_M}, 0, \ldots, 0].$$

This Poisson solver was also validated independently, by comparing the numerical solution with eigenfunctions of the Laplace operator in a rectangle.

APPENDIX B

NUMERICAL SCHEME FOR SOLVING THE SOLUTE TRANSPORT PROBLEM

We now describe the numerical method used for solving concentration equations (4.1)-(4.2). We discretize the time variable in the following way: $t_n = n\Delta t$, where $\Delta t = 2\pi/M$. We discretize the interval $0 \leq \xi \leq 1$ by defining a regular grid of the form

$$\xi_j = j\Delta\xi, \quad j = 0,\ldots,N+1, \text{ with } \Delta\xi = \frac{1}{N+1}.$$

We discretize the interval $-3 \leq \eta \leq 3$ by defining a regular grid which consists of three sections:

1. $\eta_i = -3 + i\Delta\eta, \quad i = 0,\ldots,N+1$, where $\Delta\eta = \frac{2}{N+1}$. The values of the tissue concentration, $\theta(\xi_j, \eta_i, t_n)$, in the region $0 \leq \xi \leq 1$, $-3 \leq \eta \leq -1$, are stored in the first $N+2$ rows of a matrix $\{S_{pq}\}$, $1 \leq p \leq N+2$, $1 \leq q \leq N+2$.

2. $\eta_i = -1 + i\Delta\eta, \quad i = 0,\ldots,N+1$, where $\Delta\eta = \frac{2}{N+1}$. The values of the channel concentration $C(\xi_j, \eta_i, t_n)$, in the region $0 \leq \xi \leq 1$, $-1 \leq \eta \leq 1$, are stored in the rows $N+3,\ldots,2N+4$ of the matrix $\{S_{pq}\}$, $N+3 \leq p \leq 2N+4$, $1 \leq q \leq N+2$.

3. $\eta_i = 1 + i\Delta\eta, \quad i = 0,\ldots,N+1$, where $\Delta\eta = \frac{2}{N+1}$. The values of the tissue concentration, $\theta(\xi_j, \eta_i, t_n)$, in the region $0 \leq \xi \leq 1$, $1 \leq \eta \leq 3$, are stored in the rows of $2N+5,\ldots,3N+6$ the matrix $\{S_{pq}\}$, $2N+5 \leq p \leq 3N+6$, $1 \leq q \leq N+2$.

We will see below that the advantage of using this grid is that the boundary condition (4.6)-(4.7) will not alter the tri-diagonal structure of the matrix resulting from the discretization of the concentration equations. We use the notation $D^k_\xi f^n_{ij}$ to mean the central difference approximation of the k-th order ξ-derivative of f at $\eta = \eta_i$, $\xi = \xi_j$ and $t = t_n$. The same

symbol, with a bar over it will mean a forward difference approximation and the symbol with a bar under it will mean a backward difference approximation.

We first explain the discretization of the problem for the tissue concentration, and then we explain the differences for the discretization of the channel concentration. The tissue concentration equation (4.2) is

$$\theta_t - \xi\frac{\dot{b}}{b}\theta_\xi - \eta\frac{\dot{a}}{a}\theta_\eta = \frac{1}{Pe}\left(\frac{\delta^2}{b^2}\theta_{\xi\xi} + \frac{1}{a^2}\theta_{\eta\eta} - \lambda\theta\right). \tag{B.1}$$

By denoting the coefficient in front of θ_ξ by g_{ij}^n, and defining the quantities $\alpha^+ = \max\{\alpha, 0\}$ and $\alpha^- = \min\{\alpha, 0\}$ for any real number α, we can write the first order upwind finite difference approximation of the advective term $\xi\frac{\dot{b}}{b}\theta_\xi$ as

$$(g_{ij}^n)^+\underline{D_\xi}\theta_{ij}^n + (g_{ij}^n)^-\overline{D_\xi}\theta_{ij}^n.$$

We discretize the tissue concentration equation (B.1) with a two-step ADI scheme as follows: during the first step of the calculation for each i we take the i-th row of the matrix of unknowns S and we solve for the vector of unknowns $S_p = (S_{p2}, \ldots, S_{pN+1})$ at time $t_{n+1/2}$. The discrete form of equation (B.1) is

$$\frac{\theta_{ij}^{n+1/2} - \theta_{ij}^n}{\Delta t/2} = 2\mathscr{L}_u\theta_{ij}^{n+1/2} + \frac{\delta^2}{Pe\, b_{n+1/2}^2}D_\xi^2\theta_{ij}^{n+1/2} + \frac{1}{Pe\, a_n^2}D_\eta^2\theta_{ij}^n - 2\lambda\theta_{ij}^{n+1/2}, \tag{B.2}$$

where $\mathscr{L}_u$ is the first order upwind finite difference approximation of the advective terms in (B.1). For each i, equation (B.2) holds for $j = 1, \ldots, N$. Together with the homogeneous Neumann boundary conditions at $\xi = 0$ and $\xi = 1$ this results in N equations for the unknown vector $S_p^{n+1/2} = (S_{p2}, \ldots, S_{pN+1})$ at time $t_{n+1/2}$ given information at time t_n. The system can be written in matrix form as follows

$$AS_p^{n+1/2} = \mathscr{L}_1 S_p^n + \mathscr{L}_2 S_p^n, \tag{B.3}$$

where the operator $\mathscr{L}_2$ comes from the terms defined at time t_n in equation (B.2) which do not come from $\mathscr{L}_1\theta_{ij}^n$. The matrix A is time dependent, tri-diagonal and diagonally dominant. We solve the system (B.3) by an LU factorization with recursive back substitution. When $N+3 \leq p \leq 2N+4$, the changes that come from the channel concentration equation (4.1), which is

$$C_t + \xi(U - \frac{\dot{b}}{b})C_\xi - \frac{1}{a}(V + \eta\dot{a})C_\eta = \frac{1}{Pe}\left(\frac{\delta^2}{b^2}C_{\xi\xi} + \frac{1}{a^2}C_{\eta\eta}\right), \tag{B.4}$$

are that the coefficients in front of the advective terms are different from those in (B.1) and there is no λ term. Thus, the matrix B which results from the discretization of (B.1) has the same properties of A.

The second step of the ADI scheme consists of the following: for each q, $2 \leq q \leq N+1$, we take the qth-column of S and solve for the vector of unknowns $S_q = (S_{2q}, \ldots, S_{3N+5\ q})$ at time t_{n+1}. The discrete form of (B.1) is now

$$\frac{\theta_{ij}^{n+1} - \theta_{ij}^{n+1/2}}{\Delta t/2} = \frac{\delta^2}{Pe\ b_{n+1/2}^2} D_\xi^2 \theta_{ij}^{n+1/2} + \frac{1}{Pe\ a_{n+1}^2} D_\eta^2 \theta_{ij}^{n+1}. \tag{B.5}$$

All the non-diffusive terms have not been included in this step since they were included in equation (B.2). The discrete form of the interfacial boundary conditions (4.6)-(4.7) is

$$\frac{\theta_{N+2\ j}^{n+1} - \theta_{N+1j}^{n+1}}{\Delta\eta} = \frac{a_{n+1}}{\kappa}(C_{N+3\ j}^{n+1} - \theta_{N+2\ j}^{n+1}), \tag{B.6}$$

at $\eta = -1$, and

$$\frac{\theta_{N+4\ j}^{n+1} - \theta_{N+3j}^{n+1}}{\Delta\eta} = \frac{a_{n+1}}{\kappa}(C_{N+3\ j}^{n+1} - \theta_{N+2\ j}^{n+1}), \tag{B.7}$$

at $\eta = 1$. Equation (B.5) holds for $2 \leq q \leq N+1$, $2 \leq p \leq N+1$ and $2N+6 \leq p \leq 3N+5$. In the second step of this numerical scheme the discrete form of (B.4) has the same form of (B.5), thus equations (B.6)-(B.7) together with (B.5) and the homogeneous Dirichlet conditions at $\eta = \pm 3$, result in $3N+4$ equations for the unknown vector $S_q^{n+1/2} =$

$(S_{2q},\ldots,S_{3N+5\,q})$ at time t_{n+1} given information at time $t_{n+1/2}$. The matrix $\widehat{A}$ resulting from writing the system in matrix form is also time dependent, tri-diagonal and diagonally dominant.

Due to the difficulty of finding a test solution for the problem given by equations (4.1)-(4.2) and boundary conditions (4.4), (4.3), (4.6), (4.7) and (4.13), we validate the code in the following way: we separate the domain of the problem in three parts, two corresponding to the tissue wall and one corresponding to the channel. In this way we can compare the numerical solution with an eigenfunction which satisfies one of the decoupled concentration equations in one of the three regions, satisfying appropriate boundary conditions.

If $\Delta_1 = \Delta_2 = 0$ the concentration equations (4.1)-(4.2) are reduced to

$$C_t = \frac{1}{Pe}\left(\delta^2 C_{\xi\xi} + C_{\eta\eta}\right), \tag{B.8}$$

$$\theta_t = \frac{1}{Pe}\left(\delta^2 \theta_{\xi\xi} + \theta_{\eta\eta} - \lambda\theta\right). \tag{B.9}$$

Accordingly we set initial and boundary conditions in the numerical scheme by employing the eigenfunctions

$$f_1(\xi,\eta,t) = \cos(\frac{\pi}{2}\xi)\sin(\pi\eta)\exp\left(-\frac{\pi^2}{Pe}\left(\frac{\delta^2}{4}+1\right)t\right), \tag{B.10}$$

valid on the region $0 \le \xi \le 1$, $-1 \le \eta \le 1$,

$$f_2(\xi,\eta,t) = \cos(\pi\xi)\exp(\sqrt{\lambda}(1-\eta))\exp\left(-\frac{\delta^2\pi^2}{Pe}t\right), \tag{B.11}$$

valid on the region $0 \le \xi \le 1$, $1 \le \eta < +\infty$ and

$$f_3(\xi,\eta,t) = \cos(\pi\xi)\exp(\sqrt{\lambda}(1+\eta))\exp\left(-\frac{\delta^2\pi^2}{Pe}t\right), \tag{B.12}$$

valid on the region $0 \leq \xi \leq 1, -\infty < \eta \leq -1$.

Next we calculate the solution to (B.8) numerically and we compare it to the eigenfunction f_1 for increasing values of the number of discretization points. Here we use the same number of points for the ξ and η variables. A similar comparison is performed between the solution to (B.9) and f_2 in the region $0 \leq \xi \leq 1, 1 \leq \eta \leq 3$. We can see a Log-log plot of the errors in Figure B.1. Both numerical solution are first order accurate.

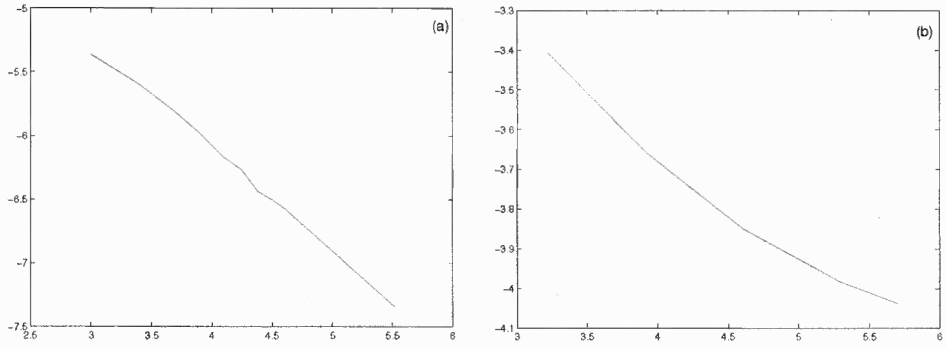

Figure B.1 Log-log plot of the error as a function of the number of discretization points. (a) accuracy of the scheme in the channel region, (b) accuracy in the tissue region.

The accuracy of the numerical scheme is calculate in the results of Figure B.1 which show logarithmic plots of the errors between the exact and computed solution versus the mesh size. The first order accuracy of the algorithm is confirmed by these results.

APPENDIX C

NUMERICAL SCHEME FOR CALCULATING u_0

We discretize the time variable in the following way: $t_n = n\Delta t$, where $\Delta t = 2\pi/M$. We discretize the interval $-1 \leq \eta \leq 1$ by defining a regular grid of the form

$$\eta_i = i\Delta\eta, \quad i = 0,\ldots,N+1, \text{ with } \Delta\eta = \frac{1}{N+1}.$$

We use the notation $D_\eta^k f_i^n$ to mean the central difference approximation of the k-th order η-derivative of f at $\eta = \eta_i$ and $t = t_n$.

A suitable numerical scheme for solving the inhomogeneous linear equation

$$u_{0t} = -1 - \frac{f_\eta}{a}u_0 + (f + \eta\dot{a})\frac{u_{0\eta}}{a} + \frac{1}{Ra^2}u_{0\eta\eta}, \quad u_0(\pm 1,t) = 0, \tag{C.1}$$

is the Crank-Nicholson scheme. Accordingly we discretize the equation as follows:

$$\frac{1}{\Delta t}(u_{0_i}^{n+1} - u_{0_i}^n) = \frac{1}{2}\left(\mathscr{L}u_{0_i}^{n+1} + \mathscr{L}u_{0_i}^n\right),$$

where

$$\mathscr{L}u_{0_i}^n = -1 - \left(\frac{1}{a_n}D_\eta^1 f_i^n\right)u_{0_i}^n + \frac{1}{a_n}(f_i^n + \eta_i\dot{a}_n)D_\eta^1 u_{0_i}^n + \frac{1}{Ra_n^2}D_\eta^2 u_{0_i}^n. \tag{C.2}$$

Equation (C.2) holds for $i = 1,\ldots,N$. The homogeneous Dirichlet conditions for u_0 provide the equations $u_{0_0}^n = u_{0_{N+1}}^n$, thus there are N equations for the unknown vector $S^{n+1} = (u_{0_1}^{n+1},\ldots,u_{0_N}^{n+1})$ at time t_{n+1} given information at time t_n. The system can be written in matrix form as follows

$$AS^{n+1} = \mathbf{F}S^n, \tag{C.3}$$

where A is a tri-diagonal time dependent matrix. We solve the system (C.3) by an LU

factorization with recursive back substitution. Here we assume that a numerical approximation of the background flow f has been calculated at the discrete points f_i^n, $i = 1,\ldots,N$. Details of a numerical scheme for calculating f can be found in (Hall and Papageorgiou 1999).

REFERENCES

Ablowitz, M. J. and Fokas, A. S. (2003), *Complex Variables*, Cambridge University Press.

Aris, R. (1956), 'On the dispersion of a solute in a fluid flowing through a tube', *Proceedings of the Royal Society of London* **235**.

Batchelor, G. K. (2002), *An Introduction to Fluid Dynamics*, Cambridge University Press.

Benzi, R., Biferale, L., Sbragaglia, M., Succi, S. and Toschi, F. (2006), 'Mesoscopic modelling of heterogeneous boundary conditions for microchannel flows', *Journal of Fluid Mechanics* **548**.

Bergé, P., Pomeau, Y. and Vidal, C. (1984), *Order Within Chaos, Towards a Deterministic Approach to Turbulence.*, Wiley-Interscience.

Birkhoff, G. (1983), 'Numerical fluid dynamics', *SIAM Review* **25**.

Blyth, M. G., Hall, P. and Papageorgiou, D. T. (2003), 'Chaotic flows in pulsating cylindrical tubes: a class of exact navier-stokes solutions', *J. Fluid Mech.* **481**.

Boddington, T. and Clifford, A. A. (1983), 'The dispersion of a reactive species (atomic hydrogen) in a flowing gas', *Proc. R. Soc. Lond.* .

Bracewell, R. N. (2000), *The Fourier Transform and Its Applications*, third edn, McGraw-Hill.

Brady, J. F. (1984), 'Flow development in a porous channel and tube', *Physics of Fluids* **27**.

Brady, J. F. and Acrivos, A. (1981), 'Steady flow in a channel or tube with an accelerating surface velocity. an exact solution to the navier-stokes equations with reverse flow', *Journal of Fluid Mechanics* **112**.

Brady, J. F. and Acrivos, A. (1982*a*), 'Closed-cavity laminar flows at moderate reynolds numbers', *Journal of Fluid Mechanics* **115**.

Brady, J. F. and Acrivos, A. (1982*b*), 'Closed-cavity laminar flows at moderate reynolds numbers', *J. Fluid Mech.* .

Bundy, R. D. and Weissberg, H. L. (1970), 'Experimental study of fully developed laminar flow in a porous pipe with wall injection', *Physics of Fluids* **13**.

Carlsson, M., Cain, P., Holmqvist, C., Stahlberg, F., Lundback, S. and Arheden, H. (2004), 'Total heart volume variation throughout the cardiac cycle in humans', *Am. H. Physiol. Heart Circ. Physiol.* **287**.

Childress, S. and Dudley, R. (2004), 'Transition from ciliary to flapping mode in a swimming mollusc: Flapping flight as a bifurcation in re_ω', *Journal of Fluid Mechanics* **498**.

Choi, C. H. and Kim, C. J. (2006), 'Large slip of aqueous liquid flow over a nanoengineered superhydrophobic surface', *Phys. Rev. Lett.* **96**.

Chorin, A. and Marsden, J. (1992), *A Mathematical Introduction to Fluid Mechanics*, Springer-Verlag.

Cottin-Bizonne, C., Jean-Louis Barrat, L. B. and Charlaix, E. (2003), 'Low-friction flows of liquid at nanopatterned interfaces', *Nature Materials* **2**.

Cottin-Bizonne, C., Jurine, S., Baudry, J., Crassous, J., Restagno, F. and Charlaix, E. (2002), 'Nanorheology: An investigation of the boundary conditions at hydrophobic and hydrophilic interfaces', *European Physical Journal E* **9**.

Cox, S. M. (1991), 'Two-dimensional flow of a viscous fluid in a channel with porous walls', *Journal of Fluid Mechanics* **227**.

Crawford, J. D. (1991), 'Introduction to bifurcation theory', *Reviews of Modern Physics* **63**.

Danckwerts, P. V. (1953), 'Continuous flow systems: Distributions of residence times.', *Chem. Eng. Sci.* **1**.

Davies, J., Maynes, D., Webb, B. W. and Woolford, B. (2006), 'Laminar flow in a microchannel with superhydrophobic walls exhibiting transverse ribs', *Physics of Fluids* **18**.

Drazin, P. and Riley, N. (2006), *The Navier-Stokes Equations, A Classification of Flows and Exact Solutions*, Cambridge University Press.

Durlofsky, L. and Brady, J. F. (1984), 'The spatial stability of a class of similarity solutions', *Physics of Fluids* **27**.

Dyke, M. V. (1965), *Perturbation Methods in Fluid Mechanics*, Academic Press.

Erdelyi, A. (1956), *Asymptotic Expansions*, Dover Publications, INC.

Feigenbaum, M. (1981), 'Some formalism and predictions of the period-doubling onset of chaos', *North-Holland Mathematics Studies* **61**.

Feigenbaum, M. J. (1980), 'The transition to aperiodic behavior in turbulent systems', *Communications in Mathematical Physics* **77**.

Ferro, S. and Gnavi, G. (1999), 'Spatial stability of similarity solutions for viscous flows in channels with porous walls', *Physics of Fluids* **12**.

Franklin, J. N. (2000), *Matrix Theory*, Dover Publications, INC.

Golub, G. H., Huang, L. C., Simon, H. and Tang, W.-P. (1998), 'A fast poisson solver for the finite difference solution of the incompressible navier-stokes equations', *SIAM Journal of Scientific Computing* **19**.

Griebel, M., Dornseifer, T. and Neunhoeffer, T. (1998), *Numerical Simulations in Fluid Dynamics: A Practical Introduction*, SIAM.

Hall, P. and Papageorgiou, D. (1999), 'The onset of chaos in a class of navier-stokes solutions', *J. Fluid Mech.* **393**.

Heil, M. and Hazel, A. L. (2003), 'Mass transfer from a finite strip near an oscillating stagnation point - implications for atherogenesis', *Journal of Engineering Mathematics* **47**.

Heil, M. and Waters, S. L. (2006), 'Transverse flows in rapidly oscillating elastic cylindrical shells', *Journal of Fluid Mechanics* **547**.

Hendy, S. C. and Lund, N. J. (2007), 'Effective slip boundary conditions for flows over nanoscale chemical heterogeneities', *Physical Review E* **76**.

Hewitt, R. E. and Hazel, A. L. (2007), 'Midplane-symmetry breaking in the flow between two counter-rotating disks', *J. Eng. Math* **57**.

Holmes, M. H. (1995), *Introduction to Perturbation Methods*, Springer-Verlag.

Horvath, K. A., Smith, W. J., Laurence, R. G., Schoen, F. J., Appleyard, R. F. and Cohn, L. H. (1995), 'Recovery and viability of an acute myocardial infarct after transmyocardial laser revascularization', *Journal of the American College of Cardiology* **25**.

Huang, L. C. (1996), 'On boundary treatment for the numerical solution of the incompressible navier-stokes equations with finite difference methods', *Journal of Computational Mathematics* **14**.

Hydon, P. E. and Pedley, T. J. (1993), 'Axial dispersion in a channel with oscillating walls', *J. Fluid Mech.* **249**.

Iserles, A. (2008), *A First Course in the Numerical Analysis of Differential Equations*, second edn, Cambridge University Press.

John, F. (1986), *Partial Differential Equations*, Springer-Verlag.

Kincaid, D. and Cheney, W. (1996), *Numerical analysis*, Brooks/Cole.

King, J. R. and Cox, S. M. (2005), 'Self-similar "stagnation point" boundary layer flows with suction or injection', *Studies in Applied Mathematics* **115**.

Kunert, C. and Harting, J. (2007), 'Roughness induced boundary slip in microchannel flows', *Physical Review Letters* **99**.

Lagerstrom, P. (1988), *Matched Asymptotic Expansions: Ideas and Techniques*, Springer-Verlag.

Lauga, E. and Stone, H. A. (2003), 'Effective slip in pressure-driven stokes flow', *Journal of Fluid Mechanics* **489**.

Lima, E. L. (1999), *Curso de Análise Vol. 2*, CNPq, Brasil.

Lin, C. C. and Segel, L. A. (1974), *Mathematics Applied to Deterministic Problems in the Natural Sciences*, Macmillan Publishing Co.

Mackenzie, J. A. (2004), On the conditioning of an upwind finite-difference approximation of a convection-diffusion boundary value problem on an adaptive grid, Technical report, Department of Mathematics University of Strathclyde.

Majda, A. J. and Bertozzi, A. L. (2002), *Vorticity and Incompressible Flow*, Cambridge University Press.

Maynes, D., Jeffs, K., Woolford, B. and Webb, B. W. (2007), 'Laminar flow in a microchannel with hydrophobic surface patterned microribs oriented parallel to the flow direction', *Physics of Fluids* **19**.

Moffatt, H. K. (1963), 'Viscous and resistive eddies near a sharp corner', *Journal of Fluid Mechanics* **18**.

Moffatt, H. K. (1964), 'Viscous eddies near a sharp corner', *Archives of Mechanics* **16**.

Murray, J. D. (2003*a*), *Mathematical Biology I: An Introduction*, third edn, Springer.

Murray, J. D. (2003*b*), *Mathematical Biology II: Spatial Models and Biomedical Applications*, third edn, Springer.

Ockendon, H. and Ockendon, J. R. (1995), *Viscous Flow*, Cambridge University Press.

O'dea, R. D. and Waters, S. L. (2006), 'Flow and solute uptake in a twisting tube', *Journal of Fluid Mechanics* **562**.

Perko, L. (2001), *Differential Equations and Dynamical Systems*, Springer.

Philip, J. R. (1972), 'Flows satisfying mixed no-slip and no-shear conditions', *Journal of Applied Mathematics and Physics* **23**.

Priezjev, N. V., Darhuber, A. A. and Troian, S. M. (2005), 'Slip behavior in liquid films on surfaces of patterned wettability: Comparison between continuum and molecular dynamics simulations', *Physical Review E* **71**.

Purnama, A. (1995), 'The dispersion of chemically active solutes in parallel flow', *J. Fluid Mech.* .

Rudin, W. (1970), *Real and Complex Analysis*, McGraw-Hill.

Ruith, M. R., Chen, P. and Meiburg, E. (2004), 'Development of boundary conditions for direct numerical simulations of three-dimensional vortex breakdown phenomena in semi-infinite domains', *Computers & Fluids* **33**.

Sbragaglia, M., Benzi, R., Biferale, L., Succi, S. and Toschi, F. (2006), 'Surface roughness-hydrophobicity coupling in microchannel and nanochannel flows', *Physical Review Letters* **97**.

Sbragaglia, M. and Prosperetti, A. (2007), 'A note on the effective slip properties for microchannel flows with ultrahydrophobic surfaces', *Physics of Fluids* **19**.

Secomb, T. W. (1978), 'Flow in a channel with pulsating walls', *J. Fluid Mech.* **88**.

Smith, R. (1988), 'Entry and exit conditions for flow reactors.', *IMA J. Applied M.* **41**.

Spivak, M. (1965), *Calculus on Manifolds*, Harper Collins.

Strikwerda, J. C. (2004), *Finite Difference Schemes and Partial Differential Equations*, SIAM.

Thomas, J. W. (1995), *Numerical Partial Differential Equations, Finite Difference Methods*, Springer.

Tome, M. F. and McKee, S. (1994), 'Gensmac: A computational marker and cell method for free surface flows in general domains', *Journal of Computational Fhysics* **110**.

Trefethen, L. N. (2000), *Spectral Methods in Matlab*, SIAM.

Waters, S. L. (2001), 'Solute uptake through the walls of a pulsating channel', *J. Fluid Mech.* **433**.

Waters, S. L. (2003), 'A mathematical model for the laser treatment of heart disease', *J. Biomech* **37**.

Watson, E. B. B., Banks, W. H. H., Zaturska, M. B. and Drazin, P. G. (1990), 'On transition to chaos in two-dimensional channel flow symmetrically driven by accelerating walls', *Journal of Fluid Mechanics* **212**.

Ybert, C., Barentin, C., Cottin-Bizonne, C., Joseph, P. and Bocquet, L. (2007), 'Achieving large slip with superhydrophobic surfaces: Scaling laws for generic geometries', *Physics of Fluids* **19**.

Young, W. R. and Jones, S. (1991), 'Shear dispersion', *Physics of Fluids* **3**.

Zauderer, E. (1998), *Partial Differential Equations of Applied Mathematics*, Wiley-Interscience.